A study of satellite lines in Eu^{3+}:Y_2SiO_5

Thomas Stinson

A thesis submitted for the degree of
Bachelor of Philosophy with Honours in Physics at
The Australian National University

November, 2023

Declaration

This thesis is an account of research undertaken between February 2023 and November 2023 at the Department of Quantum Science and Technology, Research School of Physics, The Australian National University, Canberra, Australia.

Except where acknowledged in the customary manner, the material presented in this thesis is, to the best of my knowledge, original and has not been submitted in whole or part for a degree in any university.

Thomas Stinson

November, 2023

Acknowledgements

Undertaking Honours has, without a doubt, been the most challenging yet rewarding year of my life, and this thesis only exists due to the help and support I've received during the year.

Firstly, and without a doubt most importantly, I would like to thank my supervisor Rose Ahlefeldt. I have never met anyone with a greater work ethic or level of patience. It is not possible to count the hours she has put in to help me in the lab this year, and any words I write here will not do her effort justice. All I can say is simply, thank you.

I would also like to thank Matt Sellars, for his encyclopedic knowledge of all things rare earth and optics, his uncanny ability to align a laser into a cavity, and his skill at explaining complex concepts in a way that even I can understand.

I want to thank the rest of the rare earth ion group at ANU: James, Kieran, Ellen, Lara, Jack, Raiden, Paul and David. I always looked forward to our lunchtime conversations, and I'd like to particularly thank James and Kieran for their help with the laser locking analysis.

Finally, I would like to thank my friends and family for supporting me this year, especially when I've been MIA during experimental periods. I'd like to acknowledge my housemates, Will, Luke and Chris, for making our share house a fun and enjoyable sanctuary away from the stresses of Honours, and Harry and Jack, for keeping me sane on the writing grind.

Abstract

The aim of this project was to perform the basic spectroscopy of europium pair sites in Y_2SiO_5 crystal doped with Eu^{3+} ions (Eu^{3+}:Y_2SiO_5), evaluating their potential to demonstrate a two-qubit gate operation. The optical transitions of these pair sites are called satellite lines, but little is known about their properties.

A key goal of the project was to test techniques to associate observed satellite lines in Eu^{3+}:Y_2SiO_5 with their respective pair site. Excitation spectra of the $^7F_0 \rightarrow {}^5D_0$ transition were recorded at orthogonal polarisations. The polarisation dependence of satellite lines was compared to that of the two main lines in an attempt to identify the crystallographic sites of the satellite lines. There was no similarity in the properties of the main and satellite lines, suggesting the pair site ions are strongly perturbed from the isolated ions.

I measured the optical coherence times and oscillator strengths of four satellite lines and compared the measurements to the main lines to investigate whether this could be used to associate satellite lines to pair sites. The coherence times of the four satellite lines were 122 ± 9 μs, 206 ± 6 μs, 236 ± 9 μs and 299 ± 11 μs. These values were consistent with the main lines, but due to the presence of instantaneous spectral diffusion a comparison could not be made. However, the oscillator strengths of the main lines could be measured, and each satellite line had an oscillator strength similar to one of the main lines, suggesting that this technique could potentially be used to associate satellite lines to pair sites.

Of interest for quantum computing is the possibility that two of the satellite lines are caused by degenerate pair coupling, indicating a strong interaction that could be used for two-qubit gates.

Contents

Chapter 1

Introduction

Quantum computing is a developing technology with the potential to solve problems that are insoluble for classical computers [1–3]. Some of these problems include the simulation of quantum systems [4], which has applications in pharmaceutical development [5], or transportation modelling, which can optimise freight and service routes [6].

A key criterion for a system to be suitable for quantum computing is that it has coherence times on the order of 10^4 to 10^5 times longer than the time it takes to execute a quantum logic gate operation, and finding systems that satisfy this criterion is a current area of research. Rare earth ions in solids have the required long coherence times [7, 8], and so are a proposed platform for multi-qubit[1] quantum computing [9–12]. The concept of coherence time is discussed in Section 2.3.

While most research into quantum computing requires finding quantum systems that satisfy the DiVicenzo criteria [13] (a set of requirements for implementing large scale quantum computing) and are scalable to many qubits, applications exist for small quantum processors, such as making quantum networks practical and robust to errors [14]. Rare earth ions in solids are a good candidate for this application, as the qubits in the system are frequency addressed (optically), making it viable for incorporation into the current fibre optic communication infrastructure across the world. Quantum networks are also a current area of

[1] A "qubit" is the quantum computing equivalent of a classical "bit".

research, as they can be used for provably secure communication, and potentially scalable distributed quantum computing [11, 14].

In this thesis, I aim to characterise the spectroscopic and coherent properties of satellite lines in europium doped yttrium orthosilicate crystals (Eu^{3+}:Y_2SiO_5) to determine their suitability for use in a multi-qubit quantum computer. In the following section I will introduce what a satellite line is, describe the current proposed quantum computing schemes using rare earth ions in solids, and discuss how satellite lines in doped materials could solve some of the problems with the existing schemes.

1.1 Quantum computing in the rare earths

In a rare earth doped crystal, dopant ions are randomly distributed throughout the crystal, and each ion will have a resonant excitation frequency. Each ion has a homogeneous linewidth Γ_h, which characterises the width of the absorption profile for the ion. For rare earth ions in solids, this linewidth can be on the order of 100 Hz.

While an individual ion can have a narrow Γ_h, in the doped crystal each dopant ion sees a slightly different crystal environment due to strain and defects in the crystal (such as the other dopant ions). This causes the resonant frequency of each ion to be slightly shifted, and the absorption profile of the whole sample will consist of the sum of each ions homogeneous absorption profile. This is known as inhomogeneous broadening, and the width of the resultant absorption peak has an inhomogeneous linewidth Γ_{inh}. For rare earth ions in solids, the inhomogeneous linewidth can range between 10 MHz and 10 GHz [12], which is 10^5 to 10^8 times broader than Γ_h.

While most dopant ions are far away from the defects that cause inhomogeneous broadening, when a dopant ion is physically close to a defect, its resonant frequency will be largely perturbed. Sometimes, this perturbation is large enough

that the absorption frequency is now outside of the inhomogeneously broadened line, creating a small peak of absorption resolved from the main absorption line, known as a satellite line. Satellite lines in doped crystals are commonly caused by two dopant ions closely neighbouring each other, known as a pair site [15, 16]. The interaction between ions in a pair site is not well understood, and is discussed in more detail in Section 2.4.

To date, there has been only one demonstration of a two-qubit gate operation using rare earth ions in solids, a phase gate demonstrated in Eu^{3+}:Y_2SiO_5 by Longdell et al. [17]. In this quantum computing scheme, each qubit was a frequency addressed ensemble of atoms, where each ensemble was a sub-ensemble of ions prepared in the main inhomogeneously broadened line of Eu^{3+}:Y_2SiO_5. Ensemble based quantum computing creates larger signals when reading out the state of a qubit, which increases the fidelity of the readout. The ions in this system posses permanent electric dipole moments. When an ion is optically excited, it induces a linear Stark shift in the frequencies of surrounding ions. This frequency shift was used for the quantum logic gate.

While the two qubits prepared in the main line for the above demonstration of a two-qubit gate were well resolved in frequency, this did not mean that the ions in the qubits were close spatially. If we consider exciting one ion in one qubit, the linear Stark shift it induces on ions in the other qubit will depend on the location of those other ions in the sample. In other words, the interaction between that ion and the other qubit is inhomogeneous. This inhomogeneity in interaction strength applies for all ions in the first qubit relative to ions in the second qubit, and when enacting logic gates this reduces the fidelity of the operation. To overcome the inhomogeneity, Longdell et al. "distilled" the ensemble qubits to only contain ions with a fixed interaction strength relative to ions in the other qubit. This process increased the fidelity of the gate at the cost of readout signal. Signal size constraints reduced the extent to which Longdell et al. could distill the ensemble, and so only a very low fidelity two-qubit gate was demonstrated.

An alternative approach to quantum computing in a rare earth doped solid has been proposed by Wesenberg et al. [18] where each qubit is an individual ion, opposed to an ensemble of ions. In this scheme, the same interaction is used to enact gates [19], and the interaction between two qubits will be homogeneous. This system has greater scaling potential than the one described above, as it simply requires multiple individual ions to be near each other. However, the scheme requires the ability to detect a single ion, which is difficult, and the readout signals would be much smaller than those in an ensemble based scheme.

The prior two schemes for quantum computing use rare earth ion doped solids. Recently, a scheme has been proposed by Ahlefeldt et al. [14] that uses satellite lines in a stoichiometric rare earth crystal. In a stoichiometric crystal, the rare earth ions of interest are part of the host crystal, and a different rare earth ion is doped into the crystal. Host ions neighbouring a dopant ion will each have a unique optical resonant frequency shift due to the strain caused by the dopant ion, thus creating satellite lines. Each satellite line will correspond to the ensemble of host ions in the same crystallographic position relative to a dopant ion, and the host ions in one satellite line will always be in the same fixed position relative to the dopant to host ions in another satellite line. Because of this fixed distance, if an ensemble qubit is prepared in two different satellite lines, the interaction between the ions in those lines will be homogeneous. This solves the distillation issue for the ensemble scheme described for a doped crystal, while still achieving the readout benefit of an ensemble scheme.

The ensemble scheme described above has been investigated for the stoichiometric crystal $EuCl_3 \cdot 6H_2O$ by Ahlefeldt et al. [11, 20] where the interactions between host qubit ions have been characterised. One issue with this material is that it is unstable at room temperature, difficult to prepare into high quality samples, and the distances between qubit ions are greater than 6.5 Å, which is large on the scale of ion spacing in rare earth materials. As such, new materials need to be found to implement the stoichiometric computing scheme.

Currently, there is not much understanding of how rare earth ions behave when they are within 6.5 Å of each other. For the Eu^{3+}:Y_2SiO_5 sample studied in this thesis, there are fourteen possible Eu^{3+} sites within 6.5 Å of each other. This means that two ions in a pair site within this range should have much stronger interactions than those in the stoichiometric scheme. Based on this fact, satellite lines caused by pair sites in rare earth doped crystals could improve the quantum computing scheme used by Londell et al. described above. If the qubits were prepared in an inhomogeneously broadened satellite line, opposed to the main line, then the interactions would be much stronger and would also be homogeneous, removing the need for ensemble distillation. Overall, it is possible that a quantum computing scheme using satellite lines in a doped crystal would have the benefits of using an ensemble over a single instance scheme, while still having a homogeneous interaction between the qubits in a crystal that is easy to work with.

1.2 Thesis structure

In this thesis I will present the method and results of my investigation into the spectroscopic and coherent properties of satellite lines in 0.1% Eu^{3+}:Y_2SiO_5.

In Chapter 2 I will provide the background information necessary to understand the spectral and coherent properties of rare earth ions in solids, describe the sources of satellite lines in the doped sample I studied, and describe the proposed quantum computing scheme that would use these satellite lines.

In Chapter 3 I will describe the experimental techniques that were used in my investigation, such as excitation spectroscopy, coherent spectroscopy, and balanced heterodyne detection.

Chapter 4 is a self-contained chapter. The rare earth ion group at ANU recently purchased a Toptica TA-SHG pro laser and a large amount of my time was spent setting up and stabilising this laser. In Chapter 4 I will describe the

basics of Pound-Drever-Hall laser stabilisation, and present the outcome of the stabilisation, which was characterised using coherent spectroscopy.

In Chapter 5 I will describe the measurement of excitation spectra, and briefly discuss the results from these spectra.

In Chapter 6 I will present the coherence measurements made on some of the satellite lines in Eu^{3+}:Y_2SiO_5, discuss how these results relate to those in Chapter 5.

In Chapter 7 I will summarise the results of my thesis, and discuss the implications and future work that could arise from these results.

Chapter 2

Background

In this chapter, I will provide the background information necessary for understanding this thesis. I will begin by briefly introducing the rare earth ions and their properties when doped into solids. I will then frame the rest of the chapter in the context of the Eu^{3+}:Y_2SiO_5 system studied in this thesis. I will discuss the properties of europium relevant to this thesis and how satellite lines arise in the Eu^{3+}:Y_2SiO_5 system studied.

2.1 Rare earth ions

The rare earth series consists of the lanthanide period of the periodic table, yttrium and scandium. Each rare earth element is chemically and physically very similar, which is why they can substitute for each other in crystals. In crystals, the rare earths generally form 3+ ions with the valence electrons in the $4f$ orbital. Across the lanthanide period, the $4f$ orbital is filled, and the electronic configuration of each ion RE^{3+} is $[Xe]4f^n$ for n from $0 \rightarrow 14$.

The radial electron probability distribution for the $4f$ orbital is closer to the nucleus than that of the $5s$ and $5p$ orbitals. This means that the $4f$ electrons are essentially shielded from the environment by the $5s$ and $5p$ electrons, and the $5s$ and $5p$ electrons are the ones used for bonding. This electronic structure is why the rare earths are chemically similar, and why they do not interact strongly with their crystal environment.

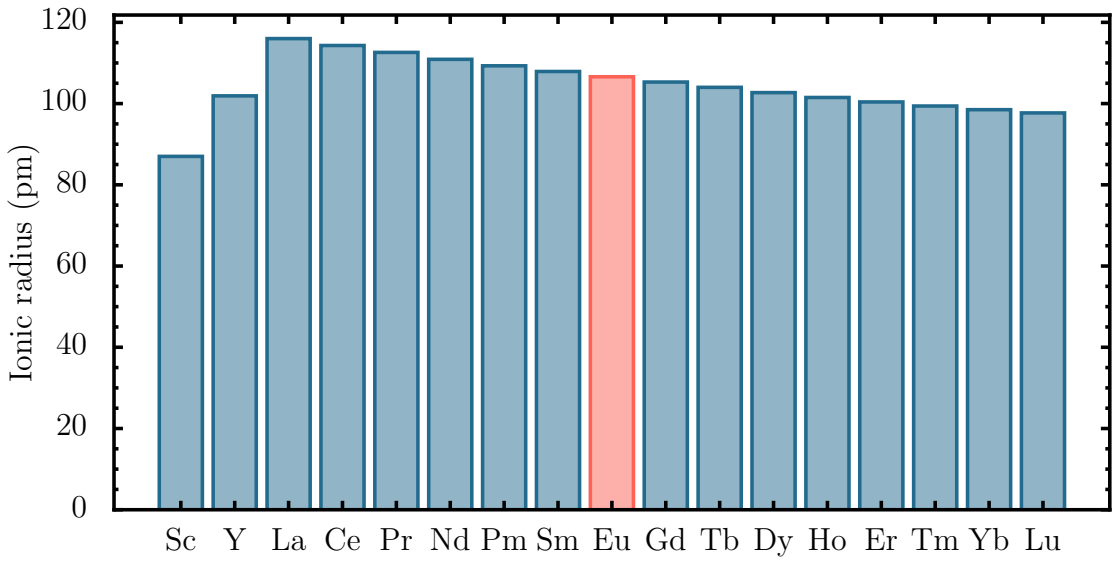

Figure 2.1: The effective ionic radii of RE^{3+} ions from [21]. Europium, the subject of this thesis, is highlighted in red.

While the $4f$ electrons are well shielded from the environment, they are not well shielded from the nucleus. Because of this, there is a steady decrease in the ionic radius of the rare earths across the lanthanide series. The differing ionic radii (shown in Figure 2.1) is the primary cause of difference in the chemistry between rare earths. When one rare earth is substituted for another in a crystalline structure, the differing radius distorts the local crystalline structure.

2.1.1 Energy level structure

The transitions of interest for quantum computing in the rare earths are those between the $4f$ levels. The shielding of the $4f$ electrons by the $5s$ and $5p$ orbitals means that Hamiltonian of a dopant rare earth ion in a crystal can be well approximated by the free ion Hamiltonian with a weak perturbation caused by the crystal field. The crystal field perturbation causes free ion energy levels with $2J + 1$ degeneracy to be split, where J is the total angular momentum quantum number. Figure 2.2 shows the energy level structure of rare earth ions doped into $LaCl_3$ that arises due to the free ion Hamiltonian and the crystal field.

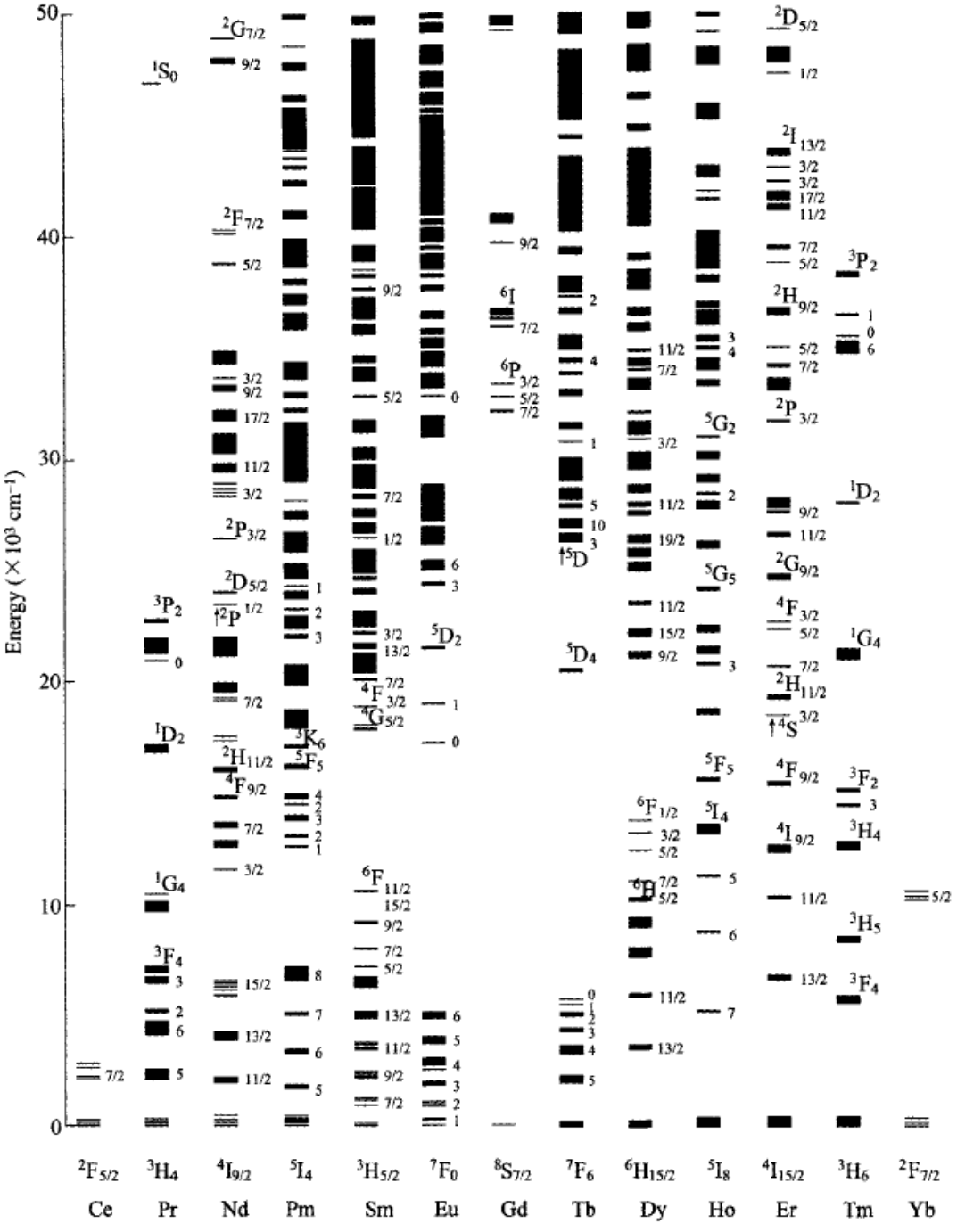

Figure 2.2: Dieke diagram from [22] showing the energy levels of RE^{3+} ions doped into $LaCl_3$. The transition studied in this thesis is the $^7F_0 \rightarrow {}^5D_0$ transition of Eu^{3+}. The thickness of the lines indicates crystal field splittings.

2.2 Properties of Eu^{3+}:Y_2SiO_5

In this thesis, I studied the $^7F_0 \rightarrow {}^5D_0$ transition of Eu^{3+} doped into Y_2SiO_5 crystal. The host crystal Y_2SiO_5 is monoclinic and belongs to the C_{2h}^6 space group. The cell parameters of Y_2SiO_5 are $a = 10.41$ Å, $b = 6.726$ Å, $c = 12.49$ Å, and $\beta = 102.65°$, where a, b and c are the crystal axes and β is the angle between a and c [23, 24]. As a monoclinic crystal, Y_2SiO_5 is optically biaxial, with one optical extinction axis aligned with the b axis, which has C_2 symmetry. The other optical extinction axes, D_1 and D_2, lie in the $a-c$ plane, where D_1 is 79° from a, 24° from c, and perpendicular to D_2. [23].

In the crystal, the Y^{3+} ions occupy two inequivalent sites, each with C_1 symmetry. When doped into Y_2SiO_5, Eu^{3+} ions substitute into one of these two sites, known as Site 1 and Site 2. The $^7F_0 \rightarrow {}^5D_0$ transition of Eu^{3+} occurs at 579.879 nm at Site 1 and 580.049 nm at Site 2 [23]. This transition is unique among the $4f$ transitions of the rare earths, as it involves a transition from a $J = 0$ ground state to a $J = 0$ excited state, which both remain as singlets after the crystal field perturbation. In higher symmetry crystals, transitions between these levels are completely forbidden [25, 26]. In Y_2SiO_5, the transition becomes weakly allowed when $J = 2$ levels are mixed into the ground state [11, 24].

The absorption coefficients α of Site 1 and Site 2 for a 0.1% Eu^{3+}:Y_2SiO_5 sample when the incident beam is polarised along the optical axes of the crystal is shown in Table 2.1. Of relevance to this thesis is the fact that the absorption polarisation dependence of Site 2 is much greater than at Site 1. This was used in Chapter 5 to try and allocate satellite lines (Section 2.4) to parent lines.

2.2.1 Hyperfine structure

The total Hamiltonian for rare earth ions in crystals is often given by [27]

$$H = H_{FI} + H_{CF} + (H_{HF} + H_Q + H_z + H_Z), \tag{2.1}$$

Polarisation	Site 1 α (cm^{-1})	Site 2 α (cm^{-1})
D_1	3.8	1.7
D_2	1.0	0.3
b	0.0	2.2

Table 2.1: The absorption coefficients α of 0.1% Eu^{3+}:Y_2SiO_5 for a beam polarised along the optical axes of the crystal. This table is reproduced from [23].

	Site 1		Site 2	
	$^{151}Eu^{3+}$ (MHz)	$^{153}Eu^{3+}$ (MHz)	$^{151}Eu^{3+}$ (MHz)	$^{153}Eu^{3+}$ (MHz)
$^7F_0$	34.544[a]	90.0	29.527[a]	76.4
	46.175[a]	119.2	57.254[a]	148.1
$^5D_0$	75	191	63	160
	102	260	108	274

Table 2.2: The hyperfine splittings of Eu^{3+}:Y_2SiO_5. This table is reproduced from [23]. Values marked with *a* are from Könz [28] and all remaining values are from Yano et al. [29, 30].

where H_{FI} is the free ion Hamiltonian, H_{CF} is the crystal field Hamiltonian, H_{HF} is the hyperfine interaction, H_Q is the electric quadrupole interaction, and H_z and H_Z are the nuclear and electronic Zeeman interactions. The bracketed terms are treated as a perturbation to the electronic energy levels in Figure 2.2 determined by the free ion and crystal field Hamiltonians, and determines hyperfine structure.

Now, Eu^{3+} has two isotopes with approximately equivalent abundance, $^{151}Eu^{3+}$ and $^{153}Eu^{3+}$. Each isotope has a nuclear spin $I = 5/2$ with a large quadrupole moment. In zero field the $^7F_0$ and $^5D_0$ energy levels are each split into three doubly degenerate hyperfine energy levels by nuclear quadrupole interactions. The splitting frequencies for Eu^{3+}:Y_2SiO_5 are shown in Table 2.2. For quantum computing applications, information is stored on the hyperfine levels of the $^7F_0$ ground state.

2.3 Lifetimes, linewidths and coherent properties

Each dopant ion in a rare earth doped crystal has a slightly different environment. This leads to broadening of the ions optical transition, where the broadening is classified by the timescale over which the broadening occurs [24].

When an optical transition is excited, it will exponentially decay back to the ground state with a time constant T_1, known as the optical lifetime that characterises the natural linewidth of the transition. This optical decay can occur radiatively with the emission of a photon, or non-radiatively, such as through coupling to phonons. Rare earth ions in solids have very long lifetimes due to their weak transition strengths [11], often on the order of seconds. In Eu^{3+}:Y_2SiO_5, the hyperfine transitions have had observed lifetimes on the order of weeks [28]. This is partly due to the fact that non-radiative decay via coupling to phonons is unlikely at the hyperfine energy levels at cryogenic temperatures (less than 4 K).

This long lifetime on the hyperfine transition is what allows Eu^{3+}:Y_2SiO_5 to spectrally holeburn so well. Spectral holeburning occurs when a transition is constantly driven by an incident beam, exciting ions from the ground state to the excited state. When the ions spontaneously decay back to the ground state, they can end up in any one of the hyperfine levels. If an ion decays back to its original state, it will get excited back to the excited state. Over time, all the ions resonant with the driven transition will be "pumped" into another hyperfine level. This issue needed to be dealt with in coherence measurements in my thesis.

The homogeneous broadening of a transition is caused by dynamic processes affecting all ions in the same way. The homogeneous linewidth Γ_h of a transition is related to the coherence time T_2 by

$$\Gamma_h = \frac{1}{\pi T_2} = \frac{1}{2\pi T_1} + \Gamma_\phi, \tag{2.2}$$

where Γ_ϕ is the contribution due to dephasing processes.

The inhomogeneous broadening of a transition is caused by static processes. For ions doped randomly into a host crystal, each ion sees a slightly different environment due to long ranging strain and defects in the crystal. These long ranging effects slightly perturb the resonant transition of each ion, creating a transition with an inhomogeneous linewidth Γ_{inh}.

For rare earth ions in solids, the inhomogeneous linewidth can range between 10 MHz to 10 GHz, while the homogeneous linewidth can be on the order of 100 Hz [12].

Coherent spectroscopy techniques, described in Section 3.2, are able to probe the homogeneous structure beneath the inhomogeneous linewidth of a transition.

2.4 Satellite lines

Satellite lines, as discussed in Section 1.1, are weak, sharp peaks of absorption resolved from the main inhomogeneously broadened line of a transition. They are commonly seen in lightly doped crystals [31] and caused by ions closely neighbouring point defects, such as rare earth impurities or other dopant ions in a sample. Close to these defects, the strain caused by the mismatch in defect and host radius causes a large enough perturbation to shift the transition beyond the inhomogeneous linewidth. Each satellite line is caused by a particular crystal environment.

Figure 2.3 is an excitation spectrum of 0.1% Eu^{3+}:Y_2SiO_5 recorded by Sellars et al. [15] that shows the satellite line structure surrounding the Site 1 and 2 main lines. Satellite lines were observed across an approximately 500 GHz range.

In doped crystals, such as Eu^{3+}:Y_2SiO_5, satellite lines can be caused by pair sites, where two dopant ions are neighbouring each other in the same fixed orientation. This concept is illustrated in Figure 2.4. In the study of Sellars et al. [15] on Eu^{3+}:Y_2SiO_5, the relative intensity of satellite ions in doped crystals

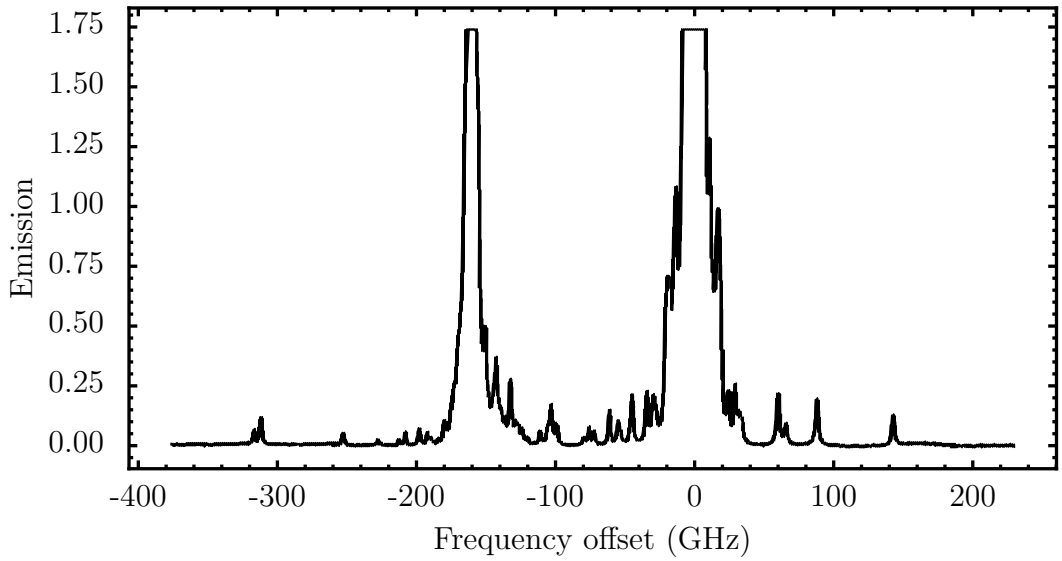

Figure 2.3: A spectrum recorded by Sellars et al. [15] showing the satellite line structure of 0.1% Eu^{3+}:Y_2SiO_5. The frequency axis shows the offset from the 579.879 nm transition of Site 1. The large peak on the negative frequency axis is the 580.049 nm of Site 2.

scaled linearly with dopant concentration, indicating that the number of pair sites was increasing quadratically with the dopant concentration, as would be expected if pair sites arose due to random doping. This scaling of satellite lines with concentration was used by Yamaguchi et al. [16] to attribute satellite lines in Eu^{3+}:$YAlO_3$ to either pair sites or other types of defect in the crystal.

The symmetries of a given crystal system can be used estimate the relative intensities of satellite lines in doped crystals [11, 32]. For the Eu^{3+}:Y_2SiO_5 crystal studied in this thesis, pair sites can either be Site 1 - Site 1 pairs, Site 2 - Site 2 pairs, or Site 1 - Site 2 pairs. Same site pair sites in this crystal can be related by C_2, inversion, or translational symmetries. In each case, the symmetries mean that the expected relative intensities of same-site pair sites to different-site pair sites should be in a 2:1 ratio [11].

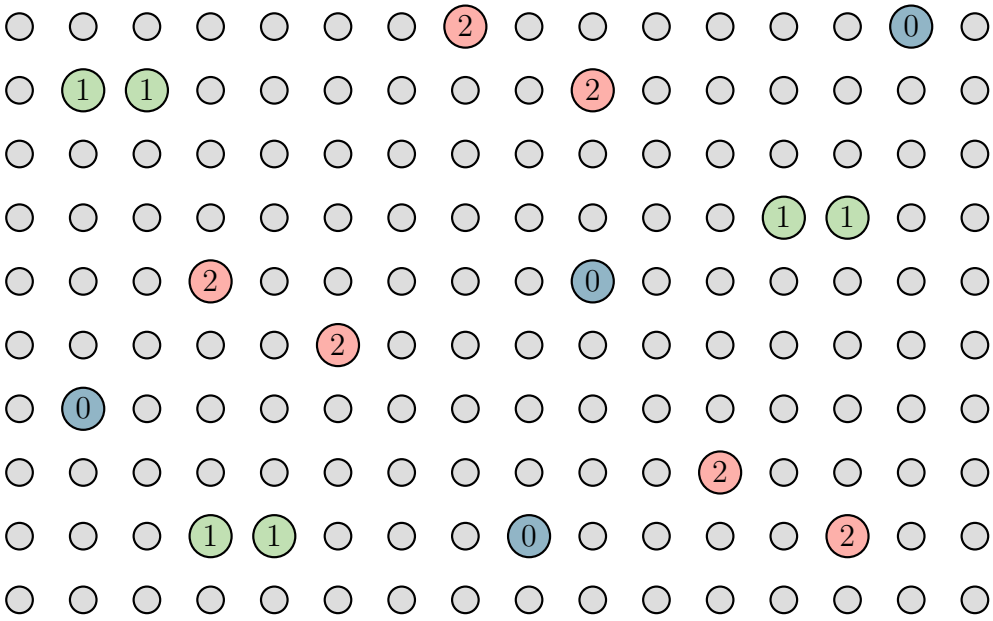

(a) Dopant ions randomly substituted into a crystal lattice. Pair sites in the same fixed orientation are indicated by the 1 and 2 ions. Each unique, fixed orientation will create a different satellite line. The 0 ions are isolated, and contribute to the main inhomogeneously broadened line.

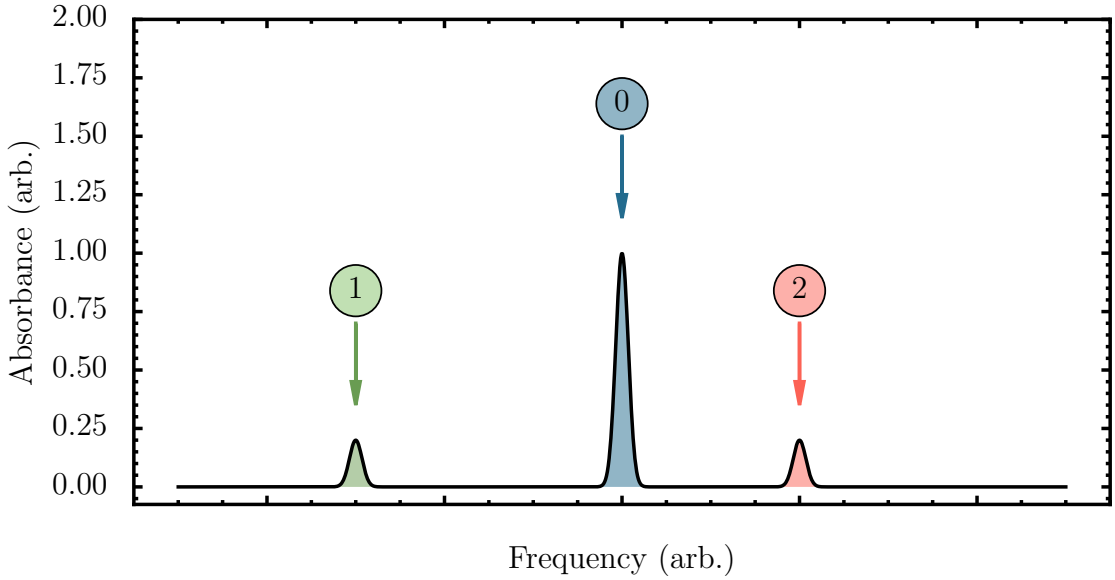

(b) The main (0) and satellite (1,2) lines caused by the randomly doped ions in (a) above. The 1 ions are closer to each other, so are more strongly perturbed and thus have a transition further from the main line compared to 2.

Figure 2.4: An illustration demonstrating how satellite lines arise in doped crystals. (a) The dopant ions substituted into the crystal lattice. (b) The main and satellite lines caused by the different crystal pair site environments.

Chapter 3

Experimental techniques

In this chapter I will briefly describe the experimental techniques used during this project. First, I will describe excitation spectroscopy, which was used to measure spectra of Eu^{3+}:Y_2SiO_5 in Chapter 5. I will then introduce the coherent measurement techniques that I used to characterise the laser in Chapter 4 and measure coherent properties of Eu^{3+}:Y_2SiO_5 in Chapter 6. This begins by introducing the Bloch vector model and optical Bloch equations. I will then describe balanced heterodyne detection, which was used to improve the coherent signals in all my experiments, and how balanced heterodyne detection of coherent signals can be used to characterise the stability of a laser. A key challenge that needed to be overcome in this project was getting signals from the satellite lines, which are weakly absorptive and emissive, and the techniques were chosen to overcome this challenge.

3.1 Excitation spectroscopy

Excitation spectroscopy measures the intensity of the *emission* from a sample while an incident laser beam is scanned in frequency. This differs from absorption spectroscopy, where the intensity of light *transmitted* through a sample is measured while a laser is scanned in frequency. As mentioned above, the satellite lines in Eu^{3+}:Y_2SiO_5 are weakly absorptive and emissive, which makes it difficult to identify a satellite line in an absorption spectrum, as it requires identifying

a small drop in transmission on a large signal. However, it is possible to detect these weak features in an emission spectrum with the use of a photomultiplier tube (PMT). The current produced at the photocathode of a PMT is linearly amplified on the order of 10^6 times by the PMT [33, 34]. The PMT also has a dark current on the order of a nano-amp [34]. Overall, a PMT makes it possible to detect an emission signal from a weak spectral feature, such as the satellite lines in Eu^{3+}:Y_2SiO_5, with a good signal to noise ratio.

Now, at a thickness z into a sample, the intensity of light at that point after some light has been absorbed can be approximated by the Beer-Lambert law,

$$I(\omega) = I_0 e^{-\alpha(\omega)z}, \tag{3.1}$$

where I_0 is the intensity of light entering the crystal, and $\alpha(\omega)$ is the absorbance profile of the sample as a function of the incident light frequency ω. For a crystal of thickness d, the total light transmitted through the crystal is given by taking $z \to d$. For the Eu^{3+}:Y_2SiO_5 sample studied in this project, the satellite lines were very weakly absorbing ($\alpha d \ll 1$). This meant it would be difficult to identify an absorption feature from a detected tranmission signal $I(\omega)$, as in this regime $I(\omega) \approx I_0$.

In emission, however, the detected signal $g(\omega)$ is given by

$$g(\omega) \propto \alpha(\omega) e^{-\alpha(\omega)z}, \tag{3.2}$$

where $\alpha(\omega)$ is again the absorbance profile of the sample, and z is the thickness into the sample from which the emission is collected [11]. In my experiments, I detected the emission from the entire thickness of the sample, as this increases

the detected signal. The shape of this signal is given by

$$\begin{aligned} G(\omega) &= \int_0^d g(\omega) dz \\ &\propto 1 - e^{-\alpha(\omega)d}, \end{aligned} \tag{3.3}$$

where d is the thickness of the sample.

Often in excitation spectroscopy, reabsorption of the emitted light by the sample can affect the lineshape of the detected signal. We did not need to consider reabsorption of the emitted light from the sample, as most of the emission from the $^5D_0$ energy level is to $^7F_2$ or higher energy levels, and occurs at > 600 nm. This also means it is possible to filter out the 580 nm laser light with a 600 nm long-pass filter before the emission reaches the PMT, preventing saturation of the PMT.

3.2 Coherent spectroscopy

To characterise the stability of the laser and measure the coherence time T_2 of the satellite lines, I used coherent spectroscopy. In coherent spectroscopy, pulses of light are used to excite transitions within a system. The coherent emission of light from the sample after the pulses is sensitive to the phase and frequency of the probed atoms, and so coherent spectroscopy can be used to study the homogeneous structure within an inhomogeneously broadened line. Before describing the coherent measurement techniques used in this thesis, I will introduce the Bloch vector model, which is often used to understand coherent spectroscopy.

The state of a two-level atom with basis states $|0\rangle$ and $|1\rangle$ and a transition dipole moment $\vec{\boldsymbol{\mu}}_{01}$ (which gives the strength of the transition $|0\rangle \rightarrow |1\rangle$) can be represented by a Bloch vector on the Bloch sphere. The Bloch sphere is a unit sphere centred at the origin in 3D Euclidean space, and any vector from the origin

to the surface of the sphere represents an atomic superposition state. The poles of the sphere along the $\pm z$-axes correspond to the $|1\rangle$ and $|0\rangle$ states respectively, the poles along the $\pm x$-axes represent the $\frac{|0\rangle \pm |1\rangle}{\sqrt{2}}$ superposition states, and the poles along the $\pm y$-axes represent the $\frac{|0\rangle \pm i|1\rangle}{\sqrt{2}}$ superposition states.

The optical Bloch equations describe the evolution of a two-level atom interacting with a classical driving field $\vec{\mathbf{E}}$. The corresponding evolution of an atom's Bloch vector on the Bloch sphere is commonly used to understand coherent transient phenomena [35]. The optical Bloch equations are given by

$$\begin{aligned} \dot{u} &= -\Delta v - \frac{u}{T_2}, \\ \dot{v} &= \Delta u + \Omega w - \frac{v}{T_2}, \\ \dot{w} &= -\Omega v - \frac{w - w_0}{T_1}, \end{aligned} \tag{3.4}$$

where u, v and w respectively correspond to the x-, y- and z-components of the atom's Bloch vector. Physically, u and v are the in- and out-of-phase components of the state with the driving field and w is the population difference between $|0\rangle$ and $|1\rangle$ [35–37]. T_1 and T_2 were introduced in Section 2.3, and correspond to the population and dephasing relaxation times respectively [36]. $\Delta = \omega_0 - \omega_{\text{light}}$ is the detuning of the driving field frequency (ω_{light}) from the resonant frequency of the transition (ω_0). Ω is the Rabi frequency of the transition, given by

$$\Omega = \frac{\vec{\boldsymbol{\mu}}_{01} \cdot \vec{\mathbf{E}}}{\hbar}. \tag{3.5}$$

Now, we can define the following vectors,

$$\begin{aligned} \vec{\mathbf{M}} &= u\hat{\mathbf{x}} + v\hat{\mathbf{y}} + w\hat{\mathbf{z}}, \\ \vec{\boldsymbol{\Omega}} &= \Omega\hat{\mathbf{x}} + 0\hat{\mathbf{y}} + \Delta\hat{\mathbf{z}}, \end{aligned} \tag{3.6}$$

where $\vec{\mathbf{M}}$ is the Bloch vector and $\vec{\boldsymbol{\Omega}}$ is known as the effective driving field. From

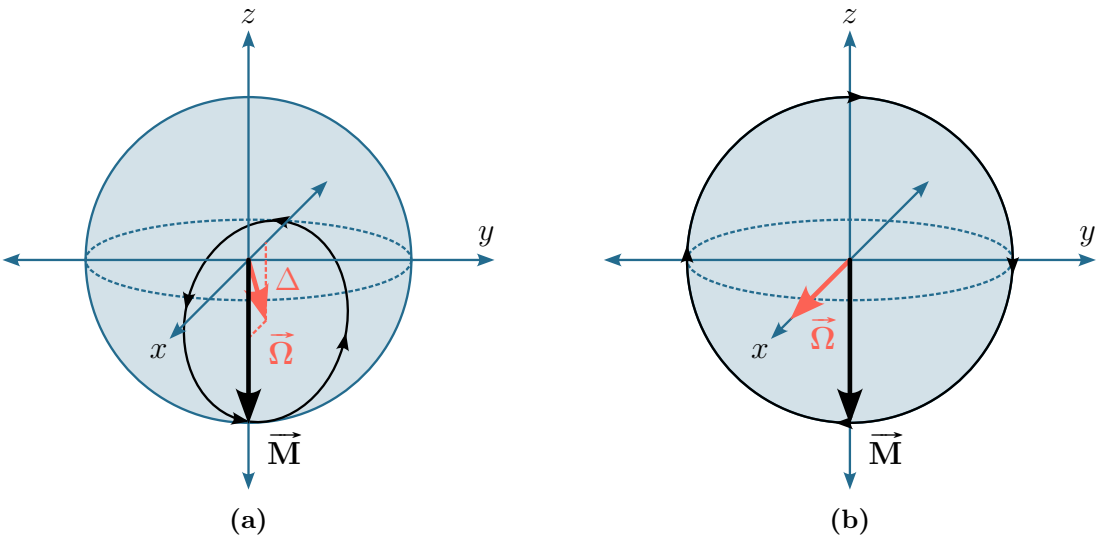

Figure 3.1: The evolution of a Bloch vector $\vec{\mathbf{M}}$ in the presence of a driving field $\vec{\mathbf{\Omega}}$. (a) The Bloch vector precessing in an off-resonant driving field ($\Delta \neq 0$). (b) The Bloch vector precessing in a resonant driving field ($\Delta = 0$).

Equation (3.4), if the relaxation terms are ignored ($T_1, T_2 \to \infty$), the evolution of $\vec{\mathbf{M}}$ under the driving field is given by

$$\frac{d\vec{\mathbf{M}}}{dt} = \vec{\mathbf{M}} \times \vec{\mathbf{\Omega}}, \tag{3.7}$$

which can be used to understand the geometric evolution of $\vec{\mathbf{M}}$ when driven by $\vec{\mathbf{\Omega}}$. Namely, Equation (3.7) states that the Bloch vector $\vec{\mathbf{M}}$ will precess in a cone about the effective driving field $\vec{\mathbf{\Omega}}$ [35]. If the driving field is resonant ($\Delta = 0$), then the axis of rotation will be in the equatorial (xy) plane of the Bloch sphere. The cases of off-resonant and resonant driving fields are shown in Figure 3.1.

If a transition is resonantly driven by a pulse of light, as opposed to a continuous field, then the Bloch vector will be rotated about the Bloch sphere by an angle $\theta = \Omega t$, where Ω is the Rabi frequency, t is the length of the applied pulse, and θ is known as the 'pulse area'. From 3.4, when the transition is not driven ($\Omega = 0$), the vector will freely precess about the z-axis of the Bloch sphere at a rate Δ. When an atom's Bloch vector has a component in the equatorial

plane, it will coherently radiate light with a phase given by its azimuthal angle, and an amplitude given by its projection in the equatorial plane. A pulse that rotates a Bloch vector into the equatorial plane of the Bloch sphere (if the vector started at $|0\rangle$) is called a $\frac{\pi}{2}$ pulse. This pulse will maximise the amplitude of the radiation, as the projection of the Bloch vector in the equatorial plane will be the entire vector.

3.3 Free induction decay

A free induction decay (FID) is a coherent transient, and its appearance can be explained with the Bloch vector model. When a short, intense pulse is applied to an inhomogeneously broadened ensemble of atoms, the ensemble will coherently radiate a light field that rapidly decays over time (the FID) once the beam is switched off [35, 38]. The radiation is at the same frequency as the atoms resonant frequency. The reason for this is as follows. The pulse will resonantly excite a frequency subensemble of atoms given by the Fourier-limited width of the pulse, meaning a short pulse will resonantly excite a wide range of atoms, and a long pulse will excite a narrow range of atoms.

If we assume that the pulse is a $\frac{\pi}{2}$ pulse, then the Bloch vector of each resonantly excited atom will be rotated into the equatorial plane of the Bloch sphere, as seen in Figure 3.2a. Once the pulse is switched off, the Bloch vectors will freely precess around the z-axis of the Bloch sphere according to their detuning Δ, as seen in Figure 3.2b. Due to their different frequencies, the radiated light fields will gradually get out of phase with each other. Since the total radiation detected from the subensemble is the coherent sum of the radiation from each atom. Over time, the detected intensity from the subensemble will exponentially decay, as the dephasing in the radiation from each atom causes destructive interference. The timescale of the decay is determined by the frequency width of the excited ensemble and therefore the original pulse. So, the FID for a short

excitation pulse decays more quickly than for a long pulse.

3.3.1 Delayed free induction decay

If a spectral hole is burned into an ensemble of atoms and a short, intense $\frac{\pi}{2}$ pulse is applied at some time τ after the hole was burned, where $T_2 \ll \tau \ll T_1$ (where T_1 and T_2 were defined in Section 2.3), then a coherent transient known as a delayed FID will be produced [27, 39]. In a delayed FID, the coherent signal decays with a time constant proportional to the inverse width of the spectral hole, opposed to the Fourier-limited width of the $\frac{\pi}{2}$ pulse, and can decay much slower than a normal FID. Similar to a normal FID, the delayed FID has the same frequency as the spectral hole. This fact, in combination with the phase-sensitive balanced heterodyne detection described in Section 3.5, were used to characterise the stability of the Toptica TA-SHG pro laser during this project using a technique developed by Pryde et al. [40], described in Section 3.6, that uses the atoms as a frequency reference to study the laser.

3.4 Two-pulse photon echo

A two-pulse photon echo occurs when an FID is rephased after some time τ. Initially, an ensemble of atoms is excited by a $\frac{\pi}{2}$ pulse at a time $t = 0$, rotating the Bloch vectors into the equatorial plane in the same way as an FID. The Bloch vectors then freely precess about the z-axis of the Bloch sphere, radiating an FID, until some time $t = \tau$, when a π pulse is applied to the ensemble. The π pulse rotates each Bloch vector about the x-axis of the Bloch sphere, mirroring their phase. After the π pulse, the Bloch vectors freely precess about the z-axis at the same rate as before until they rephase at a time $t = 2\tau$, coherently radiating a pulse of light known as a photon echo. The entire two-pulse photon echo sequence and Bloch vector rotations are shown in Figure 3.2.

The rephasing in a two-pulse photon echo is imperfect. While the π pulse

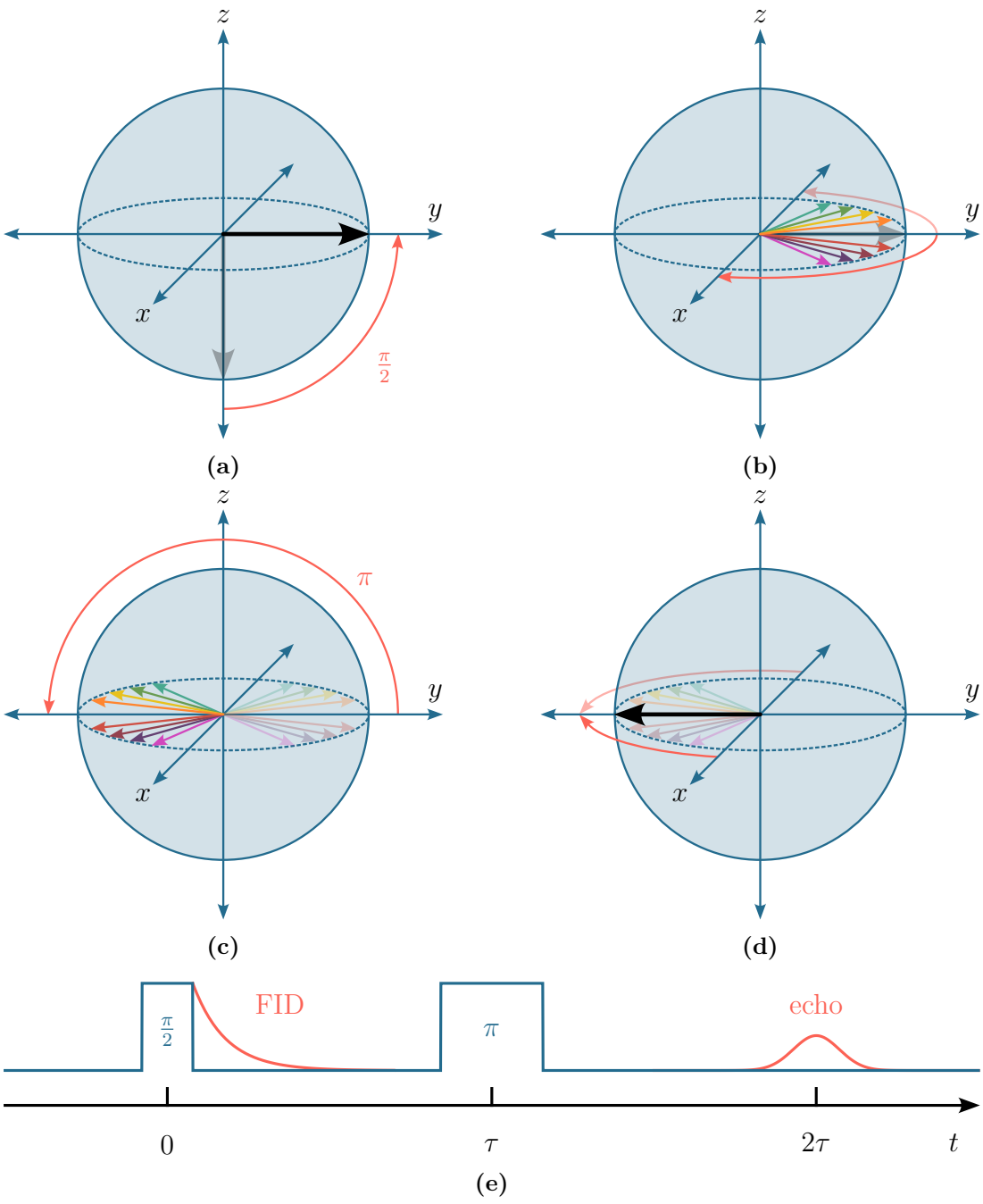

Figure 3.2: The two-pulse photon echo sequence. (a) A $\frac{\pi}{2}$ pulse at $t = 0$ rotates the Bloch vectors into the equatorial plane. (b) The Bloch vectors begin to dephase according to their detuning, producing an FID. (c) A π pulse at $t = \tau$ rotates the Bloch vectors, reversing their phase. (d) The Bloch vectors rephase, producing a photon echo at $t = 2\tau$. (e) The pulse sequence (blue) to produce an FID and photon echo and the coherent radiation (red) produced from the pulse sequence.

reverses the effects of dephasing due to detuning, it cannot reverse the effects of time-variant dephasing, such as fluctuations in the local field. Because of this, the amplitude of the echo is always less than that of the FID signal. The amplitude of a photon echo at $t = 2\tau$ after a π pulse applied at $t = \tau$ is given by

$$A(2\tau) \propto \exp\left[-\frac{2\tau}{T_2}\right], \tag{3.8}$$

where T_2 is the coherence time described in Section 2.3. By measuring the amplitude of a photon echo for increasing delay times τ, known as an echo decay, T_2 can be measured for a given spectral feature as a fitting parameter.

3.4.1 Echo area theorem

In addition to coherent properties of spectral features, we are also interested in the transition strength of the atoms creating the feature, which is characterised by the transition dipole moment $\vec{\boldsymbol{\mu}}_{01}$. This can be found from the Rabi frequency of a transition, as shown in Equation (3.5). Often, an oscillator strength is reported, opposed to the transition dipole moment. This is the transition strength relative to an oscillating electron, given by

$$f = \frac{8\pi^2 m_e c}{3e^2 h\lambda}|\vec{\boldsymbol{\mu}}_{01}|^2, \tag{3.9}$$

where m_e and e are the mass and charge of an electron, and λ is the wavelength of the light driving the transition [11].

To find the Rabi frequency of a transition and, by extension, the oscillator strength, we can utilise the echo area theorem presented by Urmancheev et. al. [41], derived from the McCall-Hahn area theorem for a pulse propagating in a two-level inhomogeneously broadened atomic ensemble [42].

The echo area for plane wave input pulses is given by,

$$\theta_e(z) = 2\arctan\left[e^{-2\tau_{12}/T_2}\sin\left(\theta_1(0)\right)\sin^2\left(\frac{\theta_2(z)}{2}\right)\sinh\left(\frac{\alpha z}{2}\right)\right], \tag{3.10}$$

where z is the propagation direction of the pulses, θ_e is the echo area, θ_1 and θ_2 are the first and second pulse areas, τ_{12} is the delay time between the first and second pulses, and α is the absorption coefficient of the ensemble. When $\theta_1 < \pi$ (which was the case for the experiments carried out in Chapter 6), the $\sin^2\left(\frac{\theta_2(z)}{2}\right)$ term is given by

$$\sin^2\left(\frac{\theta_2(z)}{2}\right) = \frac{\gamma^2}{\cosh^2\left(\beta - \frac{\alpha z}{2}\right) + \gamma^2}, \tag{3.11}$$

where β and γ are given by

$$\beta = \ln\left[\tan\left(\frac{\theta_1(0)}{2}\right)\right], \tag{3.12}$$

$$\gamma = \frac{\tan\left(\frac{\theta_2(0)}{2}\right)}{\sin\left(\theta_1(0)\right)}. \tag{3.13}$$

In the limit of $\alpha z \ll 1$ (such as echoes on the satellite lines in Eu^{3+}:Y_2SiO_5), Equation (3.10) simplifies to

$$\theta_e(z) = \alpha z \cdot e^{-2\tau_{12}/T_2}\sin\left(\theta_1(0)\right)\sin^2\left(\frac{\theta_2(0)}{2}\right). \tag{3.14}$$

To find the Rabi frequency, we can record a two-pulse echo decay, except instead of varying the delay time τ, we vary the pulse duration t for the $\frac{\pi}{2}$ and π pulses of the sequence. For square pulses of light, a pulse has an area $\theta = \Omega t$ (as discussed in Section 3.2). We can then modify Equation (3.10) (or Equation (3.14)) by substituting $2\theta_1(0) = \theta_2(0) = \Omega t$. By fitting the model to a series of echo areas with different t, the Rabi frequency Ω can be extracted as a fitting parameter.

In reality, laser beams are not plane waves, and instead have a Gaussian spatial profile. The intensity profile of a Gaussian beam is given by

$$I(r,z) = \frac{2P}{\pi w(z)^2} \exp\left(-2\frac{r^2}{w(z)^2}\right), \tag{3.15}$$

where I is the intensity, P is the total power and r is the radius of the beam from the centre [43, 44]. The term $w(z)$ is the beam radius, and is defined as the radius at which the beam intensity is $1/e^2$ of the peak intensity for some position z along the propagation direction. The reason $w(z)$ varies with z is due to diffraction, which causes the radius of a Gaussian beam to diverge. $w(z)$ is given by

$$w(z) = w_0\sqrt{1 + \left(\frac{z}{z_\mathrm{R}}\right)^2}, \tag{3.16}$$

where w_0 is the minimum radius of the beam (also known as the waist radius), and z_R is known as the Rayleigh length and is defined as the propagation position z where $w(z) = \sqrt{2}w_0$. Within the Rayleigh length either side of the beam waist, the radius of the propagating beam does not diverge significantly. For a Gaussian beam, the Rayleigh length is given by,

$$z_\mathrm{R} = \frac{\pi w_0^2}{\lambda}, \tag{3.17}$$

where λ is the wavelength of the beam. Figure 3.3 shows how the radius of a Gaussian beam evolves as it propagates.

A Gaussian spatial profile can be incorporated into Equation (3.10) by multiplying the pulses $\theta_1(0)$ and $\theta_2(0)$ by the square root of $I(r,z)$, then integrating across the area of the beam. The square root of $I(r,z)$ is used as the area of a pulse is proportional to the amplitude of a field, not the intensity. This method of incorporating the Gaussian spatial profile of the beam is valid when the thickness of the sample $d \ll z_\mathrm{R}$ of the beam, and the waist of the beam is within the sample. In this scenario, the beam does not diverge significantly when propagating

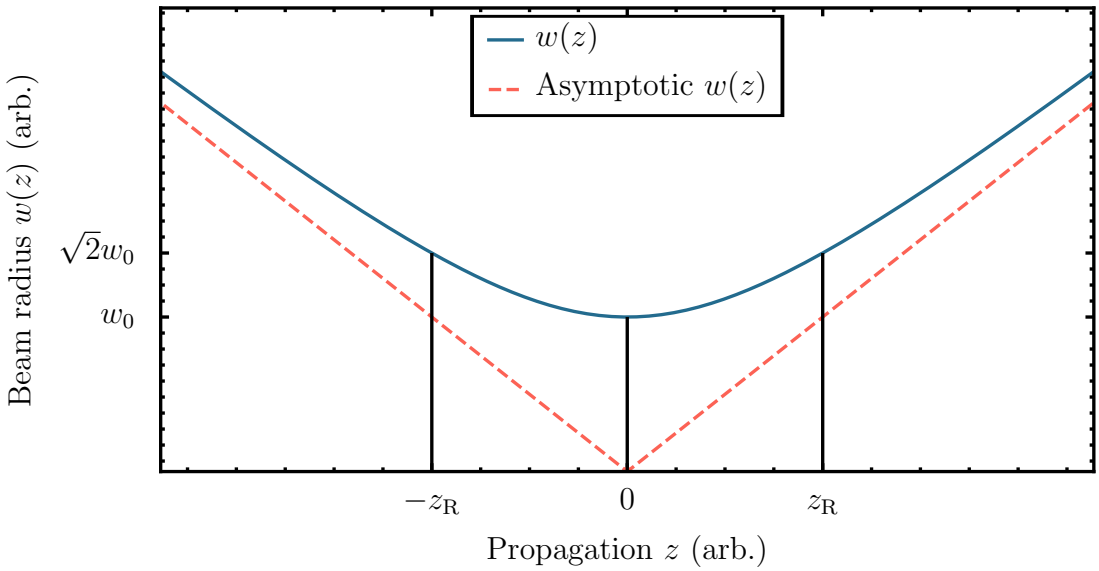

Figure 3.3: The radius $w(z)$ of a Gaussian beam (blue) near the beam waist ($z = 0$). The Rayleigh range between $\pm z_R$ indicates where the divergence of the beam due to diffraction is not significant. The red dashed line shows the behaviour of $w(z)$ when $z \gg z_R$.

through the crystal, and can be assumed to have a roughly constant waist w_0.

3.5 Balanced heterodyne detection

As mentioned in the opening paragraph of this chapter, a key challenge in investigating satellite lines in Eu^{3+}:Y_2SiO_5 will be getting signals from the satellite lines. One way to improve the signal is balanced optical heterodyne detection, which is built upon optical heterodyne detection.

In normal heterodyne detection, a weak signal is mixed with what is known as a local oscillator. The local oscillator is generally much stronger than the signal, and has an offset in frequency. In optics experiments, the mixing product is detected electronically from the superimposed waves of the signal and local oscillator when they are mode matched (have the same Gaussian beam profile or are coupled into the same single mode optical fibre).

The detected electronic signal in heterodyne detection has two components.

The first is a constant signal proportional to the total power at the detector, and the second is an oscillating beat signal with a frequency given by the frequency difference between the signal and the local oscillator. The amplitude of this beat signal is proportional to the product of the electric field amplitudes of the local oscillator and signal. This multiplication of amplitudes means that when mixed with a strong local oscillator, a weak signal can be more easily detected.

As mentioned in the previous paragraph, the detected electronic signal in heterodyne detection has a constant offset proportional to the total power at the detector. This means that any fluctuations in the intensity of a strong local oscillator will be introduced as noise on the signal. In balanced optical heterodyne detection, the combined signal and local oscillator beam is split into two paths, and the difference between the signals of the two paths is what is detected. This has the effect of suppressing the local oscillator noise [45, 46].

3.6 Delayed FIDs to characterise laser stability

FIDs and delayed FIDs can be used to characterise the stability of a laser with a technique developed by Pryde et al. [40] that uses the atoms as a frequency reference to study the laser.

For an FID or delayed FID, the signal $s(t)$ detected on an oscilloscope from a balanced heterodyne detector can be roughly approximated as

$$s(t) \approx A(t) \cos(\omega t + \phi), \tag{3.18}$$

where $A(t)$ is an exponential decay, and $\omega = 2\pi f$, where f is the frequency difference between the FID/delayed FID signal and the local oscillator.

To measure the frequency drift of a laser over different timescales, a series of FIDs and delayed FIDs can be recorded. Using a numerical Fourier transform on each shot for a given delay time, one can identify the peak central beat frequency

ω of the respective FID or delayed FID. The distribution of central frequencies tells us the average frequency drift of the laser between shots for a given delay time. If the central beat frequency itself drifts over time, this would indicate that the laser frequency is constantly drifting in one direction.

In addition to characterising the frequency stability of the laser, the phase stability of the laser can also be characterised. For a normal FID, the signal $s(t)$ can be numerically beat down in post processing. To do this, each data point can be multiplied by a complex exponential to produce a signal $S(t)$,

$$\begin{aligned} S(t) &= s(t)e^{-i\omega t} \\ &= A(t)\left[\cos(\omega t+\phi)\cos(\omega t) - i\cos(\omega t+\phi)\sin(\omega t)\right]. \end{aligned} \tag{3.19}$$

Now, we also have the trigonometric product-to-sum formulas,

$$\cos A\cos B = \frac{1}{2}\left[\cos\left(A-B\right)+\cos\left(A+B\right)\right], \tag{3.20}$$

$$\cos A\sin B = \frac{1}{2}\left[\sin\left(A+B\right)-\sin\left(A-B\right)\right]. \tag{3.21}$$

If we use Equations (3.20) and (3.21), we can expand $S(t)$, where the expansion is given by

$$S(t) = \frac{A(t)}{2}\left[\cos(\phi)+i\sin(\phi)+\cos(2\omega t+\phi)-i\sin(2\omega t+\phi)\right]. \tag{3.22}$$

If we apply a numerical low-pass filter to this signal to filter out terms with ω, the resultant signal will be given by

$$S_{LP}(t) = \frac{A(t)}{2}\left[\cos(\phi)+i\sin(\phi)\right], \tag{3.23}$$

where, if we take the phase of this signal, we will be left with the phase of the signal ϕ as a function of time. For a multiple FID measurements, the phase noise on each shot can be measured to find the average phase noise of the laser.

Chapter 4

Laser stabilisation

Most quantum logic gates require a stable laser, and this often needs to be better than the intrinsic stability of the laser. In this chapter I will describe the basic principles of Pound-Drever-Hall (PDH) laser locking, which is a laser stabilisation technique. I will then describe the method of locking the Toptica TA-SHG pro laser recently purchased by the rare earth ion group at ANU to an external Stable Laser Systems Fabry-Perot cavity with the Toptica Fast Analog Linewidth Control (FALC) pro laser locking module. The laser was purchased with the aim of eventually being used for quantum logic gates, and so its stability needed to be characterised. Afterwards, I will describe the methods and measurement of free induction decays (FIDs) and delayed FIDs in 0.1% Eu^{3+}:Y_2SiO_5. The aim of these measurements was to characterise the stability of the laser on different timescales after it was locked with the technique described in Section 3.6.

4.1 Pound-Drever-Hall locking

Pound-Drever-Hall (PDH) laser locking is a technique used for the phase and frequency stabilisation of lasers with the use of an external cavity. The technique was developed by Drever et al. [47], and in this section I will briefly describe the theory.

In PDH locking, an electro-optic phase modulator (EOM) driven by an RF source of frequency f creates frequency modulated sidebands around the laser carrier frequency at $\pm f$. Since this is only a phase modulation, the intensity of

the beam remains constant.

After the sidebands are created on the beam, the beam is coupled into an optical cavity, which acts as a frequency discriminator. When the carrier frequency is close to resonance with the cavity, the interaction breaks the symmetry of the modulation, creating an amplitude modulation in the beam reflected off the face of the cavity with a frequency f. This amplitude modulation is caused when one sideband is preferentially absorbed by the cavity compared to the other, or by the interaction of the beam with the cavity creating a phase shift in the beam. The amplitude modulated reflected beam can be detected on a photodiode and mixed with the original RF modulation. The DC component of this mixed signal can be used as an appropriate error signal for feedback control of the laser frequency.

For a beam with a carrier frequency near the resonance of the cavity, the error signal will have a steep, linear gradient through $V = 0$, where $V = 0$ occurs when the the beam is exactly on resonance with the cavity. The steepness of the gradient is inversely proportional to the linewidth of the cavity resonance. A feedback control loop can use the error signal to lock the beam frequency to peak of the cavity resonance, thus keeping the frequency stable. In other words, a feedback control loop will try to keep the error signal at 0.

4.2 Laser locking

4.2.1 Experimental setup

The experimental setup for locking the laser is shown in Figure 4.1. The box labelled “LASER” (in this and all other experimental setup diagrams) consisted of three main components: the laser head itself (Toptica TA-SHG pro), the controller for the laser head (Toptica DLC pro), and the locking electronics (Toptica FALC pro). The Toptica TA-SHG pro laser was tuned to 580 nm and under normal operation has a linewidth less than 500 kHz.

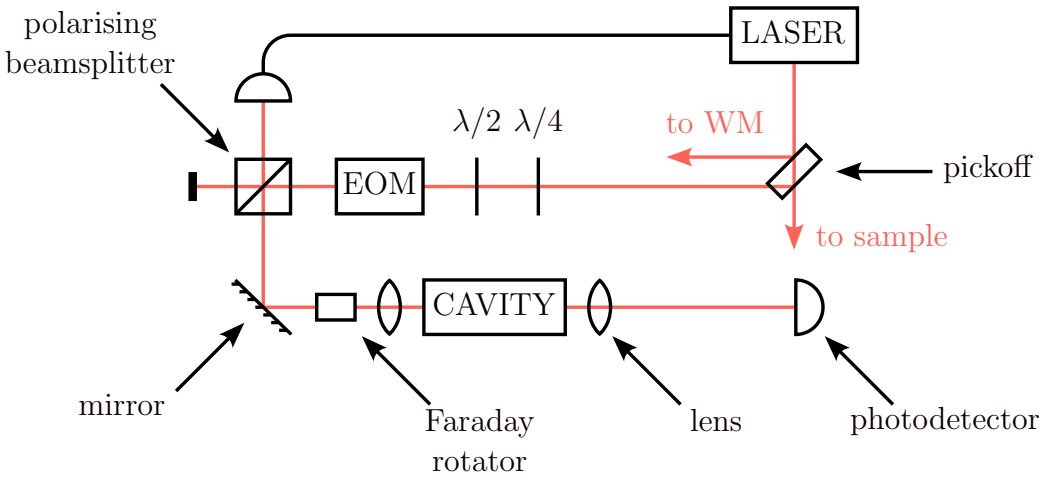

Figure 4.1: The experimental setup for the laser locking. "LASER" includes the TA-SHG pro laser head, the DLC pro laser controller, and the FALC pro laser locking module. EOM is the electro-optic modulator, WM means Wavelength Meter, $\lambda/2$ and $\lambda/4$ mean half- and quarter-wave plates.

A component of the laser beam was picked off and passed though a quarter-wave plate ($\lambda/4$) and a half-wave plate[1] ($\lambda/2$) before passing through a Thorlabs EO-PM-NR-C4 free space electro-optic phase modulator (EOM). The efficiency of the EOM and the purity of its phase modulation is dependent on the input polarisation of the beam, and so the wave plates were used to linearly vertically polarise the beam (the optimal polarisation for this EOM). The EOM was driven by a 5 MHz RF signal generated by the DLC pro laser controller. This created sidebands on the beam at ± 5 MHz from the carrier frequency, required for the generation of an error signal for PDH locking. The beam then passed through a polarising beamsplitter (PBS), which reflected the vertically polarised light from the EOM. The reflected beam was coupled into the Stable Laser Systems Fabry-Perot cavity by walking the beam with mirrors, and focusing the beam with a lens ($f = 40$ cm). The cavity has a free spectral range (FSR) of approximately 1.5 GHz, and a linewidth on the order of 100 kHz. The transmission through the cavity was focused by another lens onto a photodetector so the coupling into the primary mode of the cavity could be optimised.

[1] When used in pairs, quarter- and half-wave plates can arbitrarily rotate the polarisation of light.

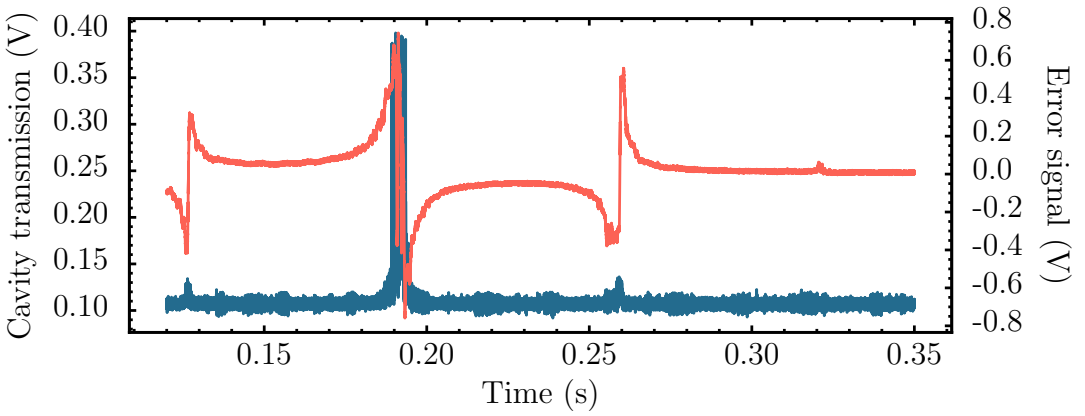

Figure 4.2: The error signal (red) generated from the locking setup. The peak cavity transmission (blue) is aligned with $V = 0$ of the signal. The frequency modulated sidebands from the EOM are also visible.

Between the PBS and the cavity was a 45° Faraday rotator. This rotated the polarisation of the beam from the PBS by 45° on its path both forwards and backwards through the rotator. This was used to horizontally polarise the reflection from the cavity on the return path to the PBS so it would be transmitted instead of reflected. This prevents the reflected beam from damaging the laser, and reduces the interference between the reflected signal and scattered light on the photodetector used for error signal generation. The signal from this photodetector was connected to the FALC locking module, which mixed it with the RF modulation to produce an error signal. An example of the error signal generated in this experiment is shown in Figure 4.2.

Associate Professor Matt Sellars helped with the coupling of the beam into the cavity and with optimisation of the error signal.

4.2.2 Experimental method

To couple the laser into the Stable Laser Systems cavity, I looked at the cavity transmission signal while the laser was scanned in frequency across a range greater than the FSR of the cavity. A cavity has multiple resonant modes dependent on the alignment and shape of the beam into the cavity. For the purposes of locking,

it is desirable to couple most of the beam into the primary mode of the cavity, and minimise coupling into other modes, as this creates the best error signal. I adjusted the alignment of the beam into the cavity until the transmission signal had large peaks corresponding to the primary mode, and very few other peaks.

To lock the Toptica TA-SHG pro laser to the external reference cavity, I incorporated the Toptica FALC pro module into the optical setup. The FALC pro module has all the electronic components required to generate an error signal for feedback control of the laser, and also implements the feedback control by modulating the voltage of a piezo[2] in the laser. To lock the laser to the cavity, I needed to find the suitable parameters for the error signal generation and feedback control for the reference cavity used in this setup.

To find the suitable error signal parameters, such as the power and phase of the original RF modulation signal being mixed back in with the reflected cavity beam for PDH locking, I looked at an oscilloscope trace of the error signal and adjusted the parameters sequentially so that the error signal had the characteristic steep linear gradient through $V = 0$ necessary for the feedback control.

After I had a suitable error signal, I looked at the cavity transmission on an oscilloscope while the laser was scanned in frequency across an approximately 2 GHz range to find at least one primary excitation mode. I adjusted the laser frequency offset until this mode was centred on the offset, and reduced the scan range to approximately 30 MHz. I then turned on the FALC pro to see the effect on the cavity transmission. For a correctly locked laser, the cavity transmission should be constant and not fluctuating. I adjusted the FALC feedback control parameters until this was the case in transmission, and then stopped the laser scanning, leaving the laser locked. For final tweaking, I looked at a real time spectrum of the error signal and adjusted the feedback parameters to reduce the low frequency noise. The final error signal and cavity transmission is shown in Figure 4.2.

[2]The piezo voltage is used to tune the Toptica TA-SHG pro beam frequency.

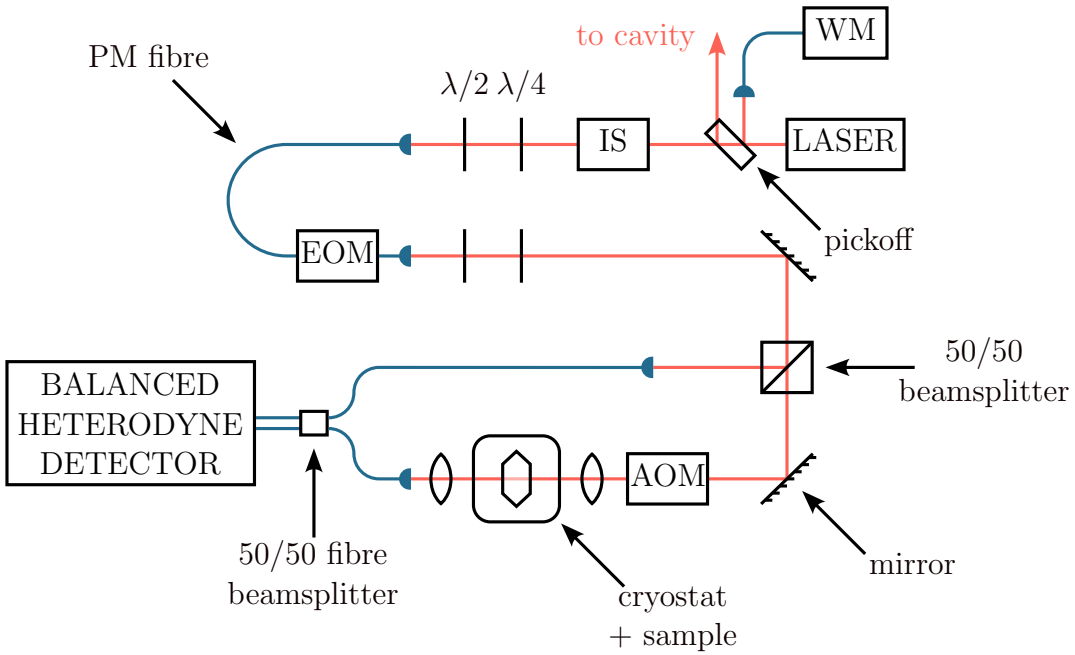

Figure 4.3: The experimental setup for the coherent spectroscopy measurements. WM is the Wavelength Meter, IS is the intensity stabilisation, EOM is the electro-optic modulator, AOM is the acousto-optic modulator, $\lambda/2$ and $\lambda/4$ mean half- and quarter-wave plates, PM means polarisation maintaining. All blue lines are single mode fibres.

4.3 Coherent spectroscopy

4.3.1 Experimental setup

The experimental setup for FID and delayed FID measurements is shown in Figure 4.3. This setup was used for all other coherence measurements in this thesis, which is why the Wavelength Meter and intensity stabiliser are included in the setup.

Two pickoffs were taken from the beam. The first pickoff was coupled into a single mode optical fibre connected to a HighFinesse Wavelength Meter WS/7 (WM) to measure the frequency of the beam. The WM had a resolution of 10 MHz, and in Chapter 5 was used as a frequency reference for the excitation spectrum of the sample. The second pickoff went to the locking setup described in Section 4.2.1.

The main beam was intensity stabilised, which was used to keep the optical power constant in Chapters 5 and 6, before being coupled into a single mode polarisation maintaining (PM) fibre connected to an AdvR KTP fibre-coupled phase modulating EOM. When a laser is locked to an external reference cavity, its frequency cannot be tuned. An EOM can be used to put frequency modulated sidebands either side of the locked beam, where the locations of the sidebands are determined by the driving frequency to the EOM. In the experiment, this allowed control of the beam frequency with the laser locked, ensuring that the desired atoms were being excited for maximum signals. The PM fibre was necessary, as the EOM is maximally efficient and maintains sideband polarisation when the beam is linearly polarised along the slow axis of its internal PM optical fibre. This maximum efficiency was necessary for detecting weak signals from satellite lines in Chapter 6. $\lambda/4$ and $\lambda/2$ wave plates before the PM fibre were used to linearly polarise the beam along the slow axis of the fibre, which is the required axis for the EOM. The EOM was driven by a combination of Windfreak SynthHD RF sources and a Moglabs Agile RF Synthesiser passed through Mini Circuits RF switches and mixers. The frequencies the EOM was driven by were on the order of 1 GHz. The switches and mixers were used for detection and burnback procedures described in Section 4.3.2.

After the EOM, the beam was launched from the PM fibre and passed through another pair of wave plates to control the polarisation of the beam into the Eu^{3+}:Y_2SiO_5 sample to optimise the coherent signal. A 50/50 beamsplitter created local oscillator and signal beam paths, where the reflected beam was coupled to a single mode fibre to be used as the local oscillator at the balanced heterodyne detector.

The signal beam passed through an IntraAction Corp. ATM-80A1 acousto-optic modulator (AOM). An AOM, when driven by an RF source, diffracts and frequency shifts an incident beam into several orders. The frequency shift of a diffracted beam is given by mf, where m is the diffraction order and f is the RF

source frequency. The ATM-80A1 AOM has a rise time on the order of 100 ns, which is short on the scale of coherent effects in Eu^{3+}:Y_2SiO_5. This means that the diffracted beams can essentially be switched on and off on the same timescale as an RF switch, and can thus be used to generate square pulses of light. The AOM in this setup was used to gate light to the sample and generate pulses. It was driven by an 80 MHz RF source and had a coupling efficiency into the first down-shifted diffraction order of approximately 75%. This diffraction order was passed through an aperture that blocked the other diffracted beams.

The beam was focused into a 0.1% Eu^{3+}:Y_2SiO_5 sample. The sample was a $5.3 \times 5.2 \times 3.8$ mm diamond-shaped crystal with polished faces along the 3.8 mm (b) axis, as shown in Figure 4.4. The sample was mounted to a sample holder and submerged in a liquid helium bath cryostat at 2 K with the b-axis aligned with the incident beam, the D_1-axis aligned horizontally to the beam (parallel to the optics table), and the D_2-axis aligned vertically to the beam (perpendicular to the optics table). The process to determine the orientation of the axes is described in Section 5.2. The beam excited the $^7F_0 \rightarrow {}^5D_0$ transition of Eu^{3+} at Site 1 to create FIDs and delayed FIDs. The transmission through the crystal was collimated and coupled into a single mode optical fibre. The signal and the local oscillator fibres were coupled into a 50/50 fibre beamsplitter for balanced heterodyne detection. The outputs from the fibre beamsplitter were coupled to a Thorlabs PDB120A balanced heterodyne detector, and signals were recorded on a TiePie HS6 computer oscilloscope.

4.3.2 Experimental method

To characterise the stability of the locked laser, I recorded FIDs and delayed FIDs. Initially, FIDs were measured with the laser scanning in frequency (not locked) to locate the frequency of the beam that would generate the best signal. To create an FID, the AOM driven by an 80 MHz RF signal gated the light to

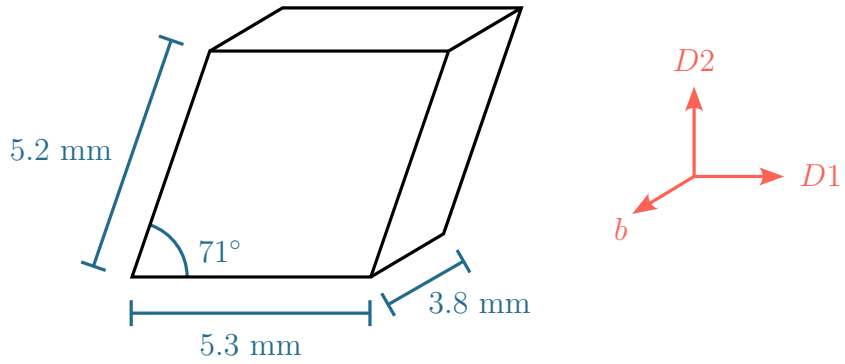

Figure 4.4: The 0.1% Eu^{3+}:Y_2SiO_5 crystal sample studied in this thesis. The blue annotations show the dimensions. The red arrows denote the optical axes. The faces aligned with the b-axis were polished.

the sample to create pulses, and the FID signal was seen on the oscilloscope.

Once the optimal frequency of the beam had been determined, the laser was locked to the external reference cavity, and the EOM was driven by an RF signal of 1 GHz by a Windfreak SynthHD frequency source to move the negative frequency modulated sideband onto resonance with the atoms. The EOM created the same frequency modulated sidebands on both the local oscillator and signal paths. The modulation frequency was chosen so the carrier beam was not exciting atomic transitions, meaning any detected FID was caused by excitation from the sideband only. For the locked laser, the AOM pulse lengths to create an FID were on the order of 100 μs. This length of pulse was optimised by repeatedly running a pulse sequence to the AOM and adjusting the length of the excitation pulse to maximise the detected signal and decrease decay time. On the timescale of the experiment, these were considered "long" pulses with a narrow Fourier-limited width, creating FIDs that had a slow decay.

The balanced heterodyne detector used in the setup had a bandwidth of 75 MHz, meaning that the 80 MHz heterodyne beat signal between the local oscillator and the signal beam after the AOM downshifted the signal beam would be inefficiently detected. To create a beat signal within the bandwidth of the detector, an RF switch changed the driving signal to the EOM from 1 GHz to

1.070 GHz after the AOM had stopped the pulse to the atoms. Increasing the RF to the EOM by 70 MHz meant that the FID signal, which had been created with sidebands on the carrier at -1.080 GHz (due to the lower frequency EOM sideband and downshifting by the AOM) would be separated from the local oscillator by 10 MHz, making it possible to detect on the heterodyne detector.

Due to the long lifetimes of the hyperfine ground state levels in Eu^{3+}:Y_2SiO_5, the laser would eventually burn a hole in the spectrum, reducing the FID signals to zero. Because of this, a burnback protocol was implemented into the method. After each FID pulse and detection, a modulated RF signal from the Moglabs Agile RF Synthesiser was mixed into the RF signal from the Windfreak SynthHD, where the combined signal drove the EOM. This modulated mixed signal caused the EOM sideband creating the FIDs to get its own sidebands, which swept outwards over the region around the spectral hole to optically pump ions back into the transition level. The burnback was on for 50 ms after each FID measurement.

Once the detection and burnback protocols had been programmed into the pulse sequence for the AOM and frequency sources, 512 FIDs were recorded with the laser locked to measure the mean phase and frequency fluctuations in the laser. After this, delayed FIDs were recorded for increasing delay times with the same detection and burnback protocol. In this case, the first pulse was on the order of 10 ms to intentionally burn a spectral hole, and the $\frac{\pi}{2}$ pulse to create the delayed FID was on the order of 1 μs. The delay times ranged from 10^{-4} to 10 s. For the shorter delay times, 512 delayed FIDs were recorded to obtain a good average for the frequency drift of the laser over that timescale. For longer delays, on the order of 100 delayed FIDs were recorded.

4.4 Results

An example of a recorded FID is shown in Figure 4.5. A zoomed in region shows the oscillating signal due to balanced heterodyne detection. The frequency

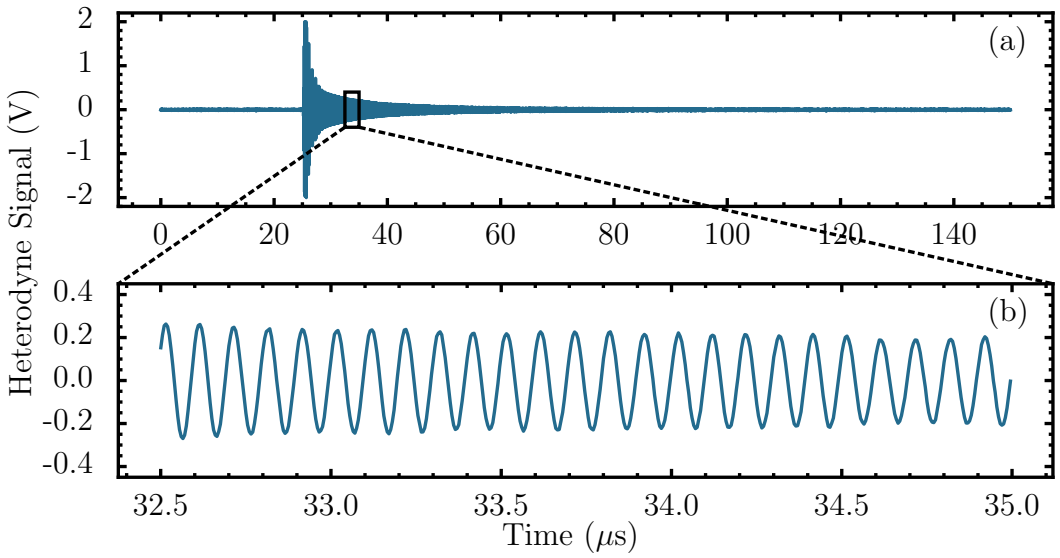

Figure 4.5: An example of a measured FID. (a) The recorded FID signal. (b) A zoomed in region of the FID signal, showing the oscillation due to the balanced heterodyne detection.

spectrum of the example FID near the expected beat frequency of 10 MHz is shown in Figure 4.6, and Figure 4.7 shows the phase of the signal across a 20 μs region found by numerically beating down the signal as described in Section 3.6. Over this region, the phase fluctuated by about 10%.

To find the mean frequency fluctuation in the laser for the recorded FIDs, I took the frequency with the largest amplitude in the frequency spectrum of a shot in the region near 10 MHz. This method is not as robust as fitting the peak, and is sensitive to amplitude noise. Most of the frequency spectra looked similar to Figure 4.6, and had relatively little amplitude noise (the small-scale structure in the spectrum). From this data, the FID signals had a mean beat frequency of 9.999 MHz with a standard deviation of 1 kHz.

To get an indication of the phase stability of the laser, I looked at a 20 μs window of the numerically beat down signal and looked at the biggest amplitude difference in that window. From this data, the laser had a mean phase drift of 0.23 ± 0.04 rad, which is an approximately 13° degree drift.

Finally, to characterise the beam stability over long timescales, the central

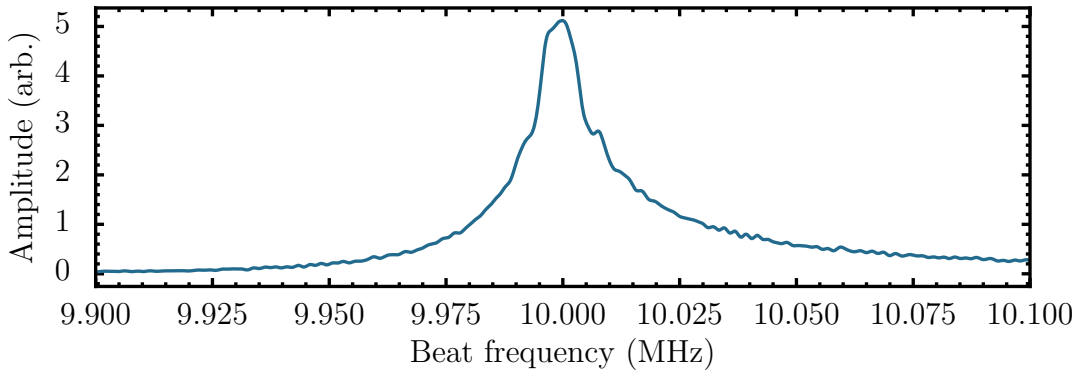

Figure 4.6: The frequency spectrum of the FID shown in Figure 4.5 near the expected beat frequency of 10 MHZ.

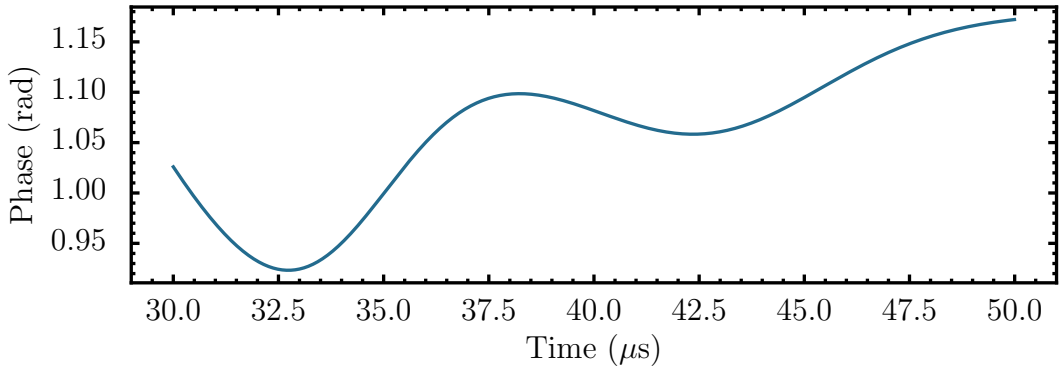

Figure 4.7: The phase of the FID shown in Figure 4.5 in a 20 μs window. In this shot, there is a roughly 10% modulation in the phase amplitude.

beat frequency of each delayed FID relative to the average FID beat frequency is shown in Figure 4.8. The mean offset and standard deviation in the offset for each delay time is shown in Figures 4.9 and 4.10 respectively.

From Figures 4.9 and 4.10, it appears that the mean beat frequency of delayed FIDs relative to the normal FIDs is roughly constant over all the delay times recorded. The standard deviations in the frequency offset for different timescales has a stepped effect with a general increasing trend. The steps could have been caused by the laser dropping lock over the course of the experiment.

In summary, the new Toptica TA-SHG pro laser was locked to an external Stable Laser Systems Fabry-Perot Cavity. This laser was purchased with the eventual goal of enacting quantum logic gate operations. For these purposes, the

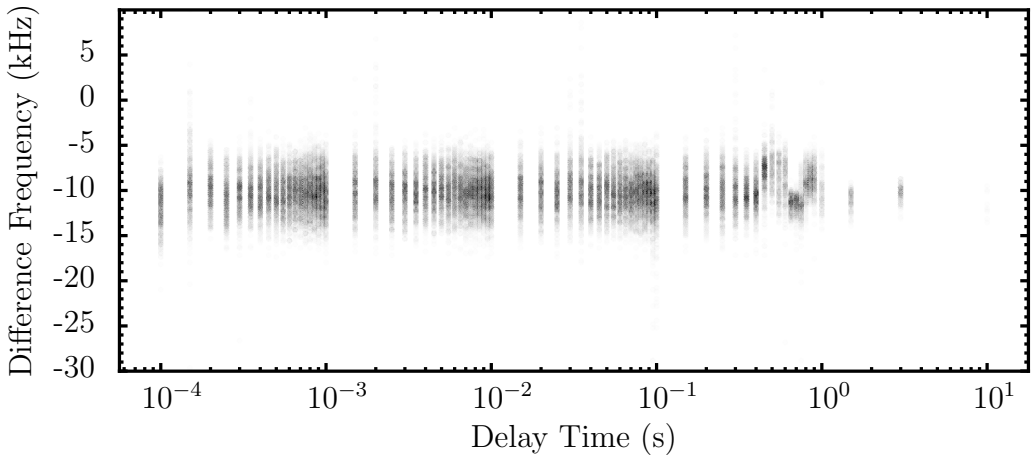

Figure 4.8: All delayed FID centres at different delay times relative to the mean FID beat frequency.

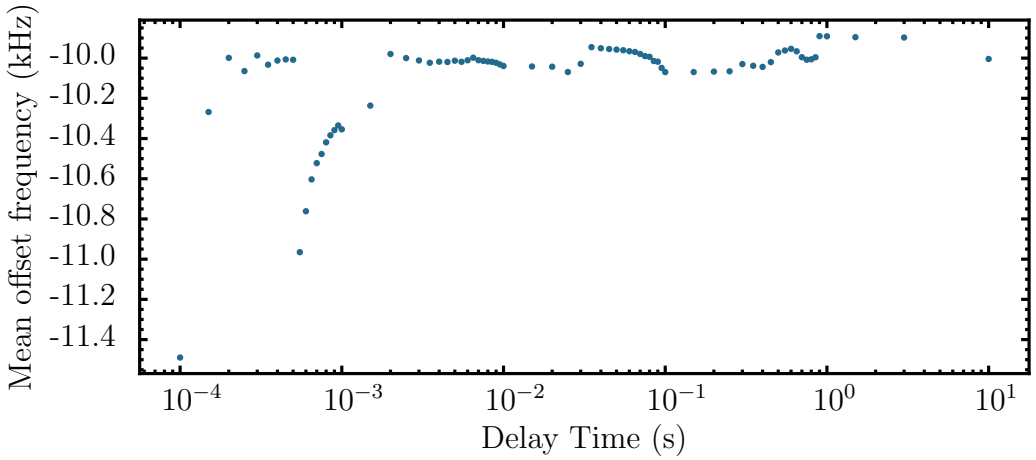

Figure 4.9: All delayed FID mean centre frequency relative to the mean FID beat frequency.

laser should be phase stable over the time to operate a gate (order of 10 μs), frequency stable over ensemble preparation times (order of 1 to 10 s) and have a linewidth less than the homogeneous linewidth over gate experiment timescales (order of 1 s) [12]. At present, this laser is likely stable enough for low fidelity two-qubit gate operations.

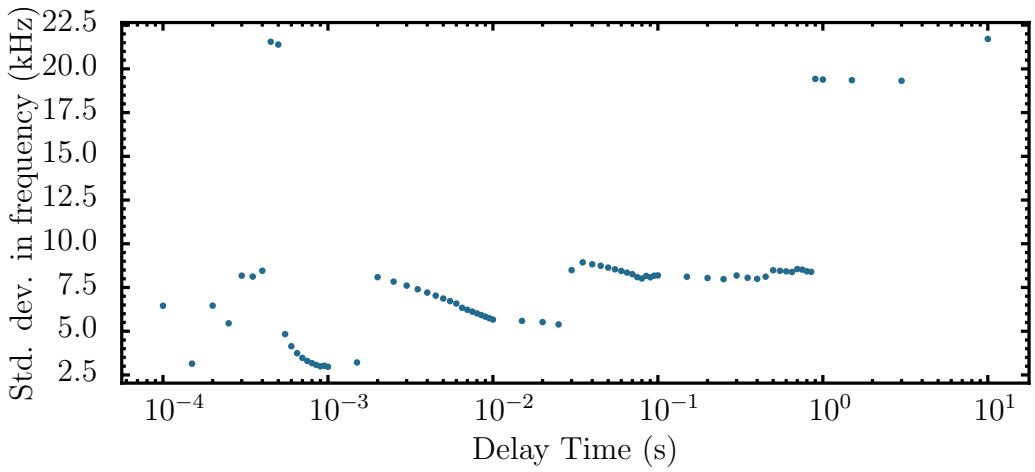

Figure 4.10: All delayed FID standard deviations in beat frequency.

Chapter 5

Excitation spectra

In this chapter, I will describe the methods and measurement of excitation spectra for the $^7F_0 \rightarrow {}^5D_0$ transition of Eu^{3+} in a 0.1% Eu^{3+}:Y_2SiO_5 sample, and discuss the results of these measurements. The aim when recording these spectra was to identify satellite lines, to determine which satellite lines were caused by same-site pair sites, and to attribute same-site pair sites to the crystallographic site that created them (Site 1 or Site 2). To do this, the polarisation dependence of the Eu^{3+}:Y_2SiO_5 spectrum was investigated by comparing spectra recorded with the incident beam linearly polarised along the D_1 and D_2 axes of the crystal respectively. Spectra were recorded for frequencies ranging between 516.3 and 517.3 THz.

5.1 Experimental setup

The experimental setup for the excitation spectra measurements is shown in Figure 5.1. Setups were shared between experiments, and so this setup is similar to the setup described in Section 4.2.1 with the inclusion of a photomultiplier tube (PMT) to detect emission. Due to the similarity of the setup, I will focus on features of the setup relevant to recording excitation spectra.

Two pickoffs were taken from the main beam from the Toptica TA-SHG pro laser tuned to 580 nm. The first pickoff was coupled into a single mode optical fibre connected to a HighFinesse Wavelength Meter WS/7 (WM) with a resolu-

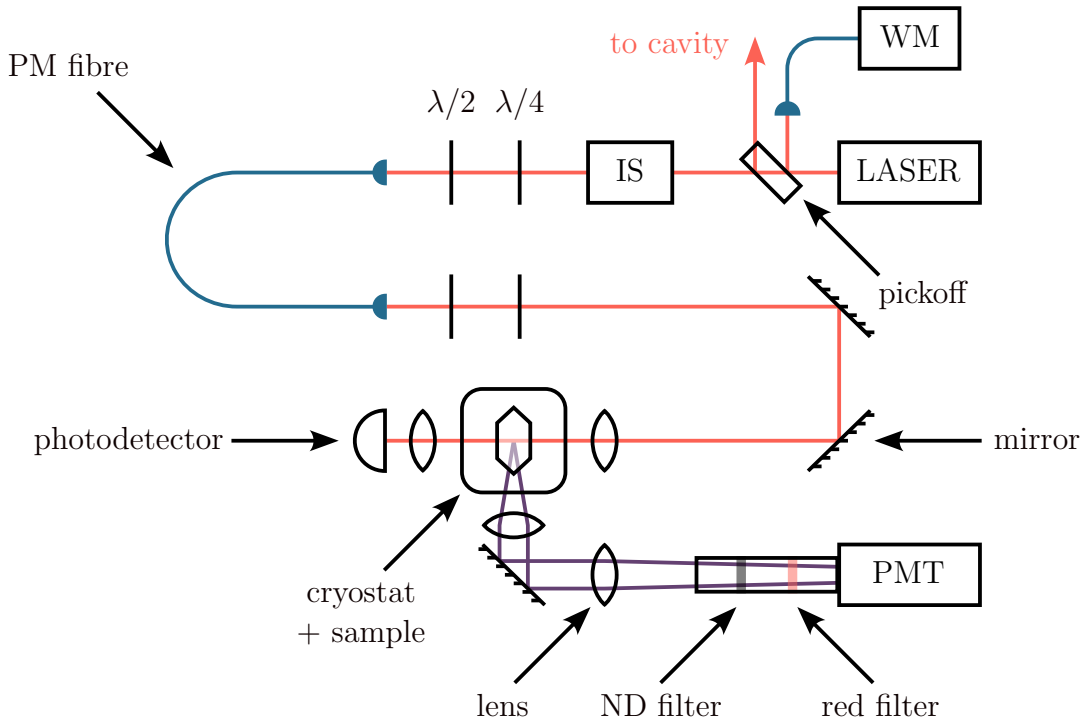

Figure 5.1: The experimental setup for excitation spectra measurements. WM is the wavelength meter, IS is intensity stabilisation, $\lambda/2$ and $\lambda/4$ mean half and quarter wave-plates, PM means polarisation maintaining, PMT is the photomultiplier tube, ND means neutral density. All the blue lines are single mode fibres.

tion of 10 MHz to record the frequency of the beam when scanning the laser to construct spectra. The second pickoff went to the locking setup used for coherent measurements.

The main beam was intensity stabilised, then passed though a quarter-wave plate ($\lambda/4$) and a half-wave plate ($\lambda/2$) before being coupled into a polarisation maintaining (PM) optical fibre (to allow the fibre-coupled electro-optic modulator used for coherent measurements to be easily integrated). The $\lambda/4$ and $\lambda/2$ wave plates before the PM fibre were used to align the beam polarisation with the slow axis of the PM fibre. For these measurements, the beam was simply relaunched from the PM fibre into free space, with polarisation controlled by $\lambda/4$ and $\lambda/2$ wave plates.

The laser beam was focused into the 0.1% Eu^{3+}:Y_2SiO_5 sample to excite the $^7F_0 \rightarrow {}^5D_0$ transition of Eu^{3+}. This was the same sample described in Section

4.3.1 (Figure 4.4), and was mounted and submerged in the same liquid helium bath cryostat. For the excitation measurements, emission was collected out the side of the cryostat and focused onto a PMT. A series of red filters were used to block scattered laser light from hitting the PMT. A neutral density (ND) filter was used to prevent saturation of the PMT when the emission from the crystal was strong, such as on the main lines.

The transmission through the crystal was collimated and recorded on a Thorlabs PDA100A-EC detector. As discussed in Section 3.1, the satellite lines were very weakly absorbing and undetectable in transmission. However, the main absorption lines were visible in transmission, and their transmission spectra were used to extract their absorbance profiles $\alpha(\omega)$. The absorbance profile was a parameter used for the fitting in Chapter 6 to calculate oscillator strengths.

A TiePie HS6 computer oscilloscope recorded the signals from the sample transmission photodetector, the PMT and the laser scan channel. The laser scan channel produces a triangle wave that tracks the laser piezo voltage during a continuous frequency sweep, and was used to align the time trace of the WM measurements with the oscilloscope signals. This was used to convert the other signals from functions of time to functions of frequency, thus creating spectra. From Sellars et al. [15], satellite structure has been seen in Eu^{3+}:Y_2SiO_5 over approximately a 500 GHz range. To create spectra with frequency ranges greater than the 50 GHz scanning range of the laser, multiple sweeps were recorded with overlapping start and end frequencies, then stitched together in post processing.

The spectra were recorded by myself, with occasional assistance from Dr Rose Ahlefeldt, and with help from Associate Professor Matt Sellars for the alignment of the beam along the slow axis of the PM fibre.

5.2 Experimental method

To address the aims of identifying satellite lines and same-site pair sites, I recorded a wide emission spectrum of the 0.1% Eu^{3+}:Y_2SiO_5 sample. For a given central frequency at a given beam polarisation, I scanned the laser in frequency and recorded the beam transmission, emission PMT signal and laser piezo voltage on an oscilloscope as described above.

To convert the signals from functions of time to functions of frequency, I used a time trace of the WM measurement. The WM does not have an analogue output signal that can be recorded on the oscilloscope. To overcome this, I wrote a script that would record timestamped data from the WM during the laser scan. Once the scan was complete, the scope trace was also saved with a timestamp. I assumed that the peaks of the piezo voltage and the peaks of the WM trace occurred at the same time, and used the timestamps to verify that this assumption was valid. In all measurements, the peaks were aligned within 10 ms, and on the timescale of a scan, which took on the order of 5 s, this assumption was valid. After this was verified, I linearly interpolated the WM data to be of equal length to the oscilloscope traces, and used this to convert my signals to functions of frequency. For each piezo scan, I recorded the signals and WM trace 4 times to obtain an average. I also recorded the power of the beam at the crystal in case the given trace needed to be normalised during stitching. I then offset the central frequency of the laser, ensuring the new range still overlapped with prior scans, and repeated the process above.

Sometimes, the emission from the crystal would saturate the PMT. In these situations, I inserted a ND filter into the path of the emission to prevent saturation. When it came to stitching the spectra together, I multiplied the emission signal by 10^{OD}, where OD is the optical density of the ND filter used.

To address the aim of attributing which satellite lines were caused by which same-site pair sites, I recorded the above spectra of the Eu^{3+}:Y_2SiO_5 sample with

the beam linearly polarised along the D_1 and D_2 axes of the crystal. With the assumption that the satellite lines behave similarly to the main lines, the theory was that same-site pair sites would have the same polarisation dependence as the crystallographic site that created them, and this could be used to attribute satellite lines to Site 1 or 2. I used crossed polarisers to determine the orientation of the optical axes of the sample. The sample was mounted such that the optical axes were aligned with either a vertically or horizontally linearly polarised beam, but initially which axis was D_1 or D_2 was unknown. Based on the measurements of Sun [23], I knew the absorbance of the sample at Site 1 should be stronger when the field is linearly polarised along D_1. I looked at the transmission through the crystal when the laser was scanned across Site 1 for both a vertically and horizontally linearly polarised beam, and determined that the D_1 axis was aligned with a horizontally polarised beam, and the D_2 axis was aligned with a vertically polarised beam.

Once I had determined the orientation of the optical axes of the crystal, I recorded spectra of the Eu^{3+}:Y_2SiO_5 sample as described above, with the beam linearly polarised along the D_1 (horizontal) and D_2 (vertical) axes of the crystal. To determine the polarisation of the beam incident on the crystal, I inserted a polarising beam splitter (PBS) into the optical path. A PBS transmits linearly horizontally polarised light, and reflects linearly vertically polarised light. To create a horizontally polarised beam, I inserted a power meter into the reflected beam from the PBS and rotated the $\lambda/4$ and $\lambda/2$ wave plates to minimise the power in the reflected beam, which corresponded to a pure horizontally polarised beam in transmission. I then removed the PBS from the setup and recorded a spectrum. To change the polarisation to vertical, I rotated the $\lambda/2$ wave plate by 45°.

While the inclusion of PM fibre simplified the inclusion of the fibre-coupled EOM for coherence measurements, it made polarisation control of the light into the sample difficult. The PM fibre had frequency dependent birefringence. This

meant that across a given laser scan, the polarisation state of the beam would drift. While a PM fibre should have no polarisation drift for a correctly polarised input beam, I was unable to perfectly align the beam to prevent the drift across the large scan range of the laser. The observed drifts were small, and corresponded to 5-10% of the orthogonal polarisation state being introduced in a given scan. However, since the frequency did drift, I performed the power minimisation technique for every scan offset before recording the spectra.

To construct a wide spectrum for each polarisation of light, I normalised all averaged spectra, based on their power and any ND filters in the path, and subtracted the background noise, which I also recorded. I then compiled the data into one large spectrum. I manually tweaked the DC offset of each individual spectrum so that the same spectral features covered by different scans would overlap each other. This was valid post-processing, as a change in the DC offset of a signal likely corresponded to a small change in the background light in the room leaking into the PMT. The spectra were recorded in darkness, but a curtain to the lab had light leaking through that could change shot to shot. Finally, I ran a numerical 20 Hz low-pass filter forwards and backwards across the final stitched spectrum to remove high frequency noise from the PMT signal.

5.3 Results

The wide spectra for the incident beam aligned along the D_1 and D_2 axes of the 0.1% Eu^{3+}:Y_2SiO_5 sample are shown in Figures 5.2 and 5.3 respectively. Marked on the two spectra are the Site 1 and 2 mains lines (S1, S2), as well as satellite lines where it was *attempted* to record coherence measurements in Chapter 6 (marked by an asterisk), and satellite lines where it *was* possible to record coherence measurements (marked by a letter A-D).

For each resolved peak, their location, heights, and ratios of heights for when the field was polarised along D_1 vs D_2 is shown in Table 5.1.

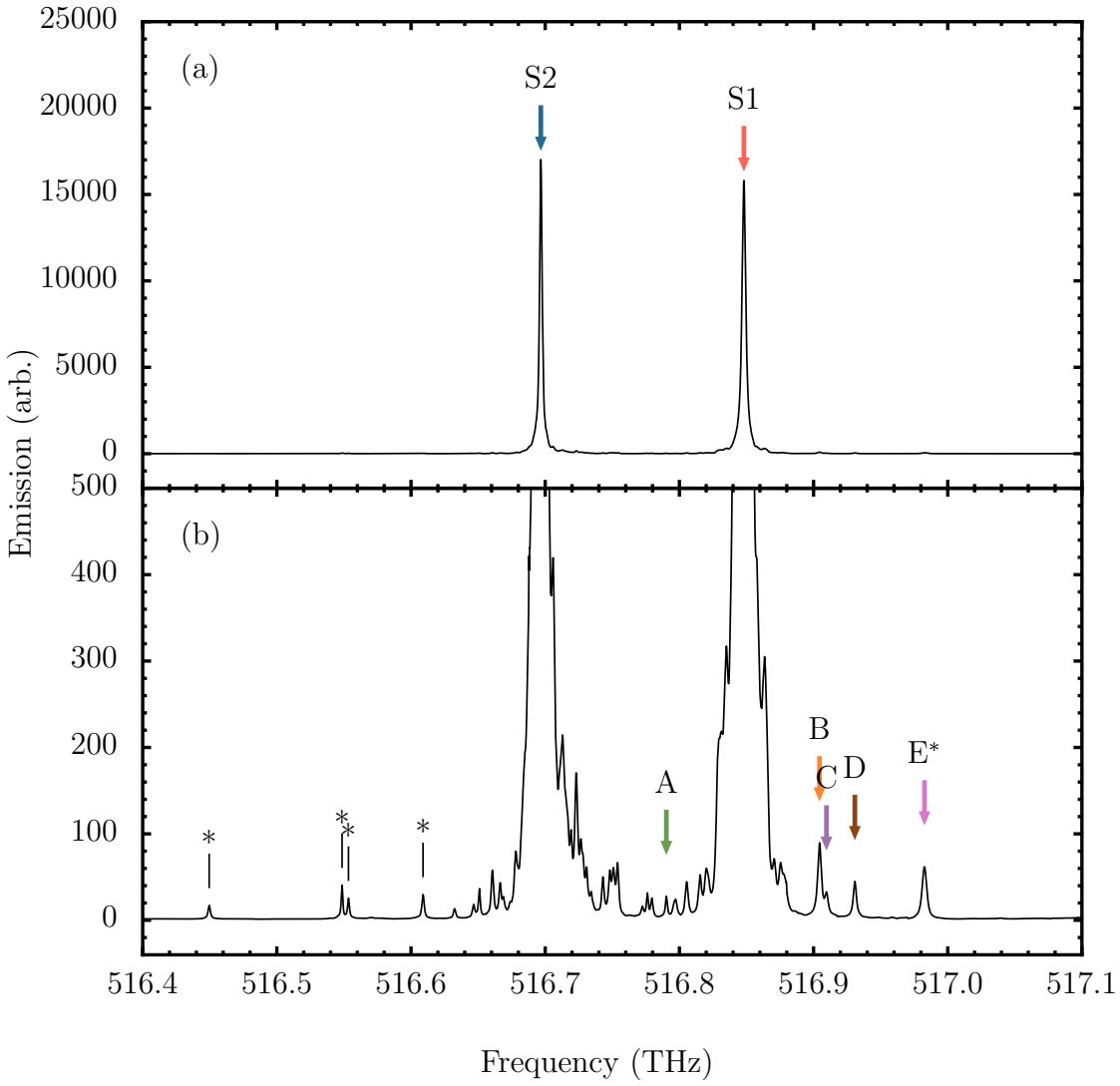

Figure 5.2: (a) An excitation spectrum of 0.1% Eu^{3+}:Y_2SiO_5 with light polarised along D_1. (b) The same spectrum as (a), zoomed in on the y-axis to show the satellite lines. The complete recorded spectrum covered 516.33445 - 517.32808 THz, but the regions beyond the above plots contained no satellite lines. The satellite line marked with the arrow (E) was recorded with unknown beam polarisation. The S1 and S2 arrows denote the Site 1 and 2 main lines. The coherence measurements described in Chapter 6 were recorded at S1, S2, and the satellite lines A-D. The satellite lines lines marked with an asterisk show where coherence measurements were attempted, but there was no signal. The locations of all the resolved peaks are shown in Table 5.1.

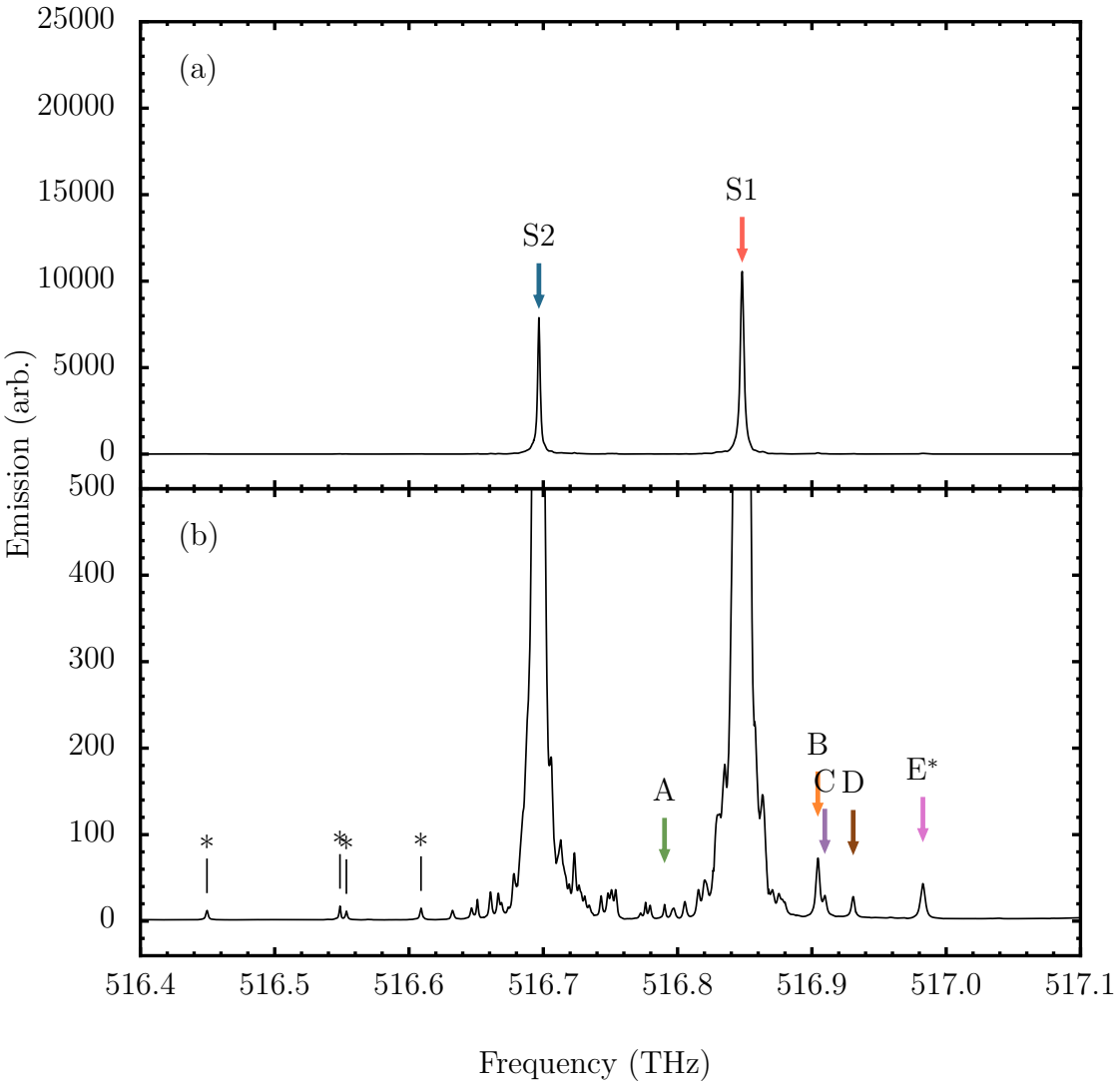

Figure 5.3: (a) An excitation spectrum of 0.1% Eu^{3+}:Y_2SiO_5 with light polarised along D_2. (b) The same spectrum as (a), zoomed in on the y-axis to show the satellite lines. The complete recorded spectrum covered 516.33445 - 517.32808 THz, but the regions beyond the above plots contained no satellite lines. The satellite line marked with the arrow (E) was recorded with unknown beam polarisation. The S1 and S2 arrows denote the Site 1 and 2 main lines. The coherence measurements described in Chapter 6 were recorded at S1, S2, and the satellite lines A-D. The satellite lines lines marked with an asterisk show where coherence measurements were attempted, but there was no signal. The locations of all the resolved peaks are shown in Table 5.1.

Frequency (THz)	D_1 Height (arb.)	D_2 Height (arb.)	Ratio D_2/D_1	Label
516.44956	17.2	12.3	0.72	*
516.54860	40.6	17.4	0.43	*
516.55338	25.6	11.5	0.45	*
516.60895	29.9	14.9	0.50	*
516.63242	13.4	12.4	0.92	
516.64662	18.4	15.2	0.83	
516.65094	36.5	25.0	0.69	
516.66062	57.9	33.7	0.58	
516.66642	43.5	32.2	0.74	
516.66881	27.4	21.4	0.78	
516.69673	17000	7880	0.46	S2
516.74300	50.3	29.2	0.58	
516.74814	58.1	32.5	0.56	
516.75077	61.0	36.2	0.59	
516.75391	66.7	36.4	0.55	
516.77612	31.6	21.6	0.68	
516.77947	25.6	18.2	0.71	
516.79028	27.8	19.2	0.69	A
516.79714	24.4	14.9	0.61	
516.80541	44.6	22.6	0.51	
516.84808	15800	10600	0.67	S1
516.90442	89.7	72.9	0.81	B
516.90962	32.8	29.7	0.90	C
516.93078	45.0	28.3	0.63	D
516.98267				E*

Table 5.1: The locations of all resolved satellite lines, their peak emission heights when the incident beam was polarised along D_1 and D_2, the ratio of the heights D_2/D_1 and their corresponding label in Figures 5.2 and 5.3.

Site	Literature			Measured		
	α of D_1 (cm^{-1})	α of D_2 (cm^{-1})	Emission D_2/D_1	α of D_1 (cm^{-1})	α of D_2 (cm^{-1})	Emission D_2/D_1
1	3.8	1.0	0.41	2.6	0.8	0.42
2	1.7	0.3	0.23	1.3	0.2	0.19

Table 5.2: The theoretical [23] and measured absorption coefficients α of 0.1% Eu^{3+}:Y_2SiO_5 at Site 1 and 2 for an incident beam polarised along D_1 or D_2. The third column of each section is the theoretical ratio of the emission peak heights for the different polarisations based on the absorption coefficients for the sample of thickness 3.8 mm studied in this experiment.

As mentioned in Section 5.2, if satellite lines have the same properties as the main lines, then the polarisation dependence of the satellite lines should be the same as the polarisation dependence of the parent line, allowing the parent to be identified. From Sun [23], I knew that the peak absorption coefficient α of 0.1% Eu^{3+}:Y_2SiO_5 at both S1 and S2 when the beam was polarised along D_1 was greater than D_2, and that S2 had a much larger drop in absorption than S1. Table 5.2 shows the literature values of α from [23], my measured values of α by fitting Equation (3.1) to the transmission signals at each site with a Voigt absorption profile, and the theoretically predicted D_2/D_1 emission height ratio from both of these cases when using Equation (3.3) for S1 and S2.

From Table 5.2, the absorption coefficients I measured for the sample were all approximately 70% of the literature values. This indicated that the Eu^{3+} concentration of my sample may have been less than the assumed 0.1% concentration. Regardless, the relatively constant change in absorption coefficient from my measurements compared to literature meant that in both cases, I expected the ratio of the S1 emission peak to have a D_2/D_1 ratio of approximately 0.4, and the S2 emission peak to have a D_2/D_1 ratio of approximately 0.2. From Table 5.1, the actual D_2/D_1 ratios of S1 and S2 were 0.67 and 0.46 respectively. The larger drop in emission for S2 compared to S1 was as expected from the literature, but the the reason why the ratios do not match the predicted ratios is unclear.

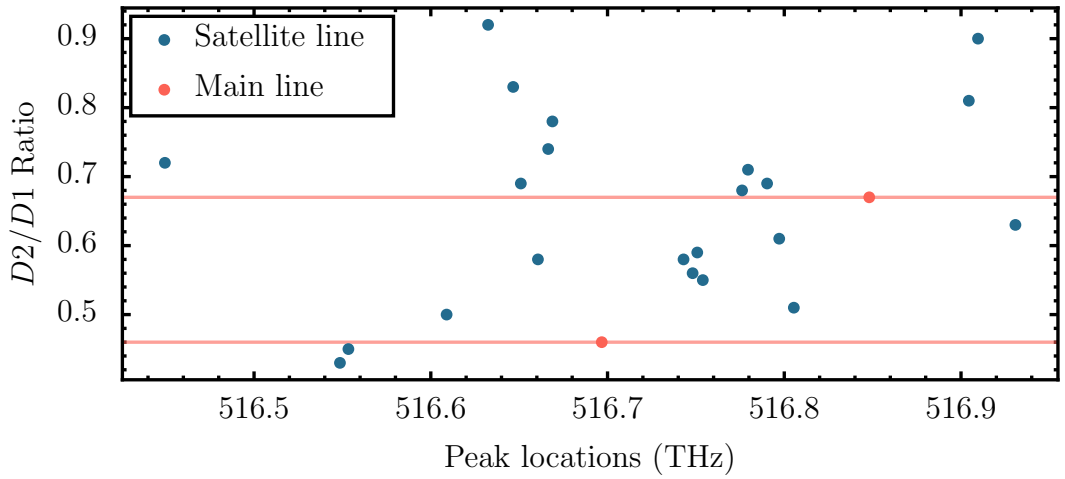

Figure 5.4: The ratios of the peak emission heights of the satellite lines (blue) and main lines (red) when the incident beam was polarised along D_2 and D_1.

Despite not knowing why the ratios of S1 and S2 were not as expected, I looked at the measured ratios of the satellite lines to see if any satellite lines shared a ratio with the measured main line ratios. The ratios are shown in Figure 5.4. From Figure 5.4, the apparently random distribution of ratios for the satellite lines, and the fact that ratios are not clustered about the 0.67 and 0.46 ratios of S1 and S2 respectively, suggests that the assumption that satellite lines have the same properties as the main lines is not valid.

In addition to investigating the polarisation dependence of the satellite lines, I also wanted to investigate the satellite line heights relative to each other. As discussed in Section 2.4, I expected the heights of the satellite lines to be determined by the site abundances, and that I could use this to identify which satellite lines were caused by same-site pair sites. For the spectrum in Figure 5.2 where the emission signals from the main lines are similar, I expected there to be two clusters of peaks heights, where one cluster was twice the height of the other, corresponding to same-site pair sites and different-site pair sites respectively. The heights of all the satellite lines where the beam was polarised along D_1 are shown in Figure 5.5.

From Figure 5.5, there is no clear indication that there are two distinct clusters

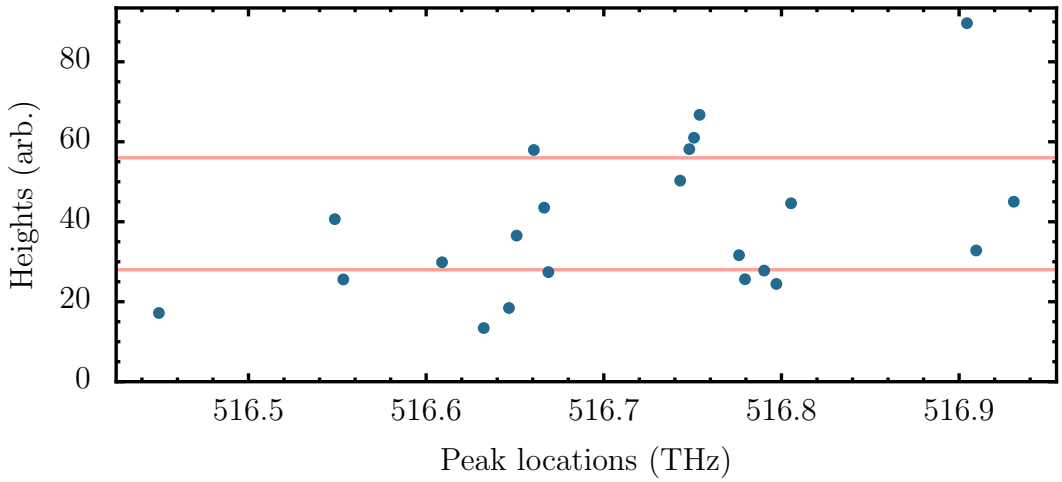

Figure 5.5: The peak emission heights of the satellite lines (blue) when the incident beam was polarised along D_1. The red lines are at heights of 28 and 56, and were adjusted by eye with the aim of hitting two clusters where one cluster had heights twice the value of the other.

of satellite line peak heights. It is possible that overlapping of peaks would cause some deviation from the expected clusters, but this cannot explain the lack of a clear trend.

In summary, I recorded wide range, high resolution spectra of Eu^{3+}:Y_2SiO_5 when the laser was polarised along the D_1 and D_2 axes of the sample. From these spectra I was able to address the aim of identifying where satellite lines are in Eu^{3+}:Y_2SiO_5, and the well resolved peak locations are shown in Table 5.1.

The polarisation spectra were used to see if the satellite lines had the same properties as the main lines. From Figure 5.4, I showed that there was no clear trend or correlation in the polarisation dependence of the satellite lines compared to the main lines. This, in conjunction with the varied heights of satellite lines in Figure 5.5, meant that I could not allocate satellite lines to their parent lines based on the measurements in this chapter. Overall, it is clear that the optical properties of the satellite lines are not similar to the main lines, and suggests that they are strongly perturbed.

Chapter 6

Coherent measurements

In this chapter, I will describe the methods for measuring the coherent properties of the main lines and some satellite lines in Eu^{3+}:Y_2SiO_5. The aim of these measurements was to understand the results from Chapter 5. Specifically, the measurements in Chapter 5 showed that the optical properties of the satellite lines in Eu^{3+}:Y_2SiO_5 are different to the properties of the main lines. To get more information about the satellite lines, I recorded the coherence time T_2 of the satellite lines, which is also crucial to determine the viability of a system for quantum computing, using the two-pulse photon echo technique described in Section 3.4. Additionally, I measured the oscillator strengths of the main and satellite lines using the technique described in Section 3.4.1 to shed more light on how satellite line properties differ to the main lines.

The experimental setup for these measurements was almost identical to the setup in Section 6.1 (Figure 4.3), with the exception that a Rigol RSA5065-TG Spectrum Analyzer was used to record the signals opposed to an oscilloscope, and the fibre-coupled electro-optic modulator (EOM) was bypassed. The reasons for these changes are discussed in Section 6.1. Due to the similarity of the experimental setup, it is not described in this Chapter.

6.1 Experimental method

To measure the coherence times T_2 and oscillator strengths on the satellite lines, I recorded two-pulse photon echo amplitudes in Eu^{3+}:Y_2SiO_5. To measure T_2,

I recorded an echo amplitude decay, where I used the two-pulse photon echo sequence described in 3.4 with fixed $\frac{\pi}{2}$ and π pulses and increasing τ. To measure the Rabi frequency, and thus oscillator strengths, I fixed τ and measured the echo amplitude with increasing pulse lengths $\frac{\pi}{2}$ and π as described in Section 3.4.1.

Initially, I followed a similar method to the one described in Section 4.3.2, where I used the EOM sidebands to excite the transitions, detect the signal, and burnback into the spectral holes created, and used the AOM to gate the pulses of light. I used a Rigol RSA5065-TG Spectrum Analyzer to detect the signals opposed to an oscilloscope, as it allowed me to average out the noise on the echo signals at the heterodyne beat frequency to improve signal detection. When an oscilloscope is used to detect a heterodyne signal, the signal average over multiple shots will tend to zero as the phase difference between shots interferes. The spectrum analyser had a noise floor on the order of -50 dBm.

When I used the EOM in the setup, I was able to see echo signals on the main lines, but there was no signal from satellite lines. As discussed in Chapter 3, the satellite lines are very weakly absorbing. Because the EOM only modulates a small fraction of the beams power into the sidebands, the interaction is very weak, and the echo is difficult to detect. Additionally, as discussed in Section 5.2, I had observed frequency dependent birefringence in the polarisation maintaining fibre coupled to the EOM. While this was not a major issue for excitation spectra, the efficiency and purity of EOM phase modulation depends on the polarisation of the input beam. Due to how weak the sidebands were relative to the carrier, there was no way to determine their polarisation after the EOM, and thus no way to optimise the polarisation into the crystal for the best signals.

To overcome the signal detection issues on the satellite lines, I bypassed the EOM entirely. This meant that the carrier was exciting the transitions for photon echo decays, and there was no way to modulate the local oscillator to create a beat at 10 MHz, as was done in Section 4.3.2. It was still possible to detect the 80 MHz beat between the echoes and local oscillator on the balanced heterodyne

detector despite it only having a bandwidth of 75 MHz.

While bypassing the EOM made it possible to detect photon echoes from satellite lines, this method meant that there was no way to control the frequency of a locked laser or burnback spectral holes with the EOM as was done in Section 4.3.2. As such, all photon echo measurements were recorded with the laser scanning across an approximately 500 MHz range with a frequency of 0.5 Hz. This scanning meant that holes were constantly being burned back into, maintaining signals. This scanning method for detection would be an issue in a gate operation sequence, where a lasers frequency stability is important.

Once signals were being detected on satellite lines, I ran two pulse photon echo sequences on the marked lines in Figure 5.2. Some satellites, marked with an asterisk, showed no signals. For the echo amplitude decays, I optimised the lengths of the $\frac{\pi}{2}$ and π pulses and adjusted the beam polarisation to maximise the signal before recording the amplitudes. For each delay time or pulse length, I averaged the signal 64 times to both reduce the noise and average out the effects of the scanning laser.

In order to eventually extract the oscillator strengths from a Rabi frequency, the amplitude of the beam field needed to be known. This amplitude can be found by taking the square root of a beams intensity profile, given by Equation (3.15). To find the intensity profile of the beam, which is dependent on the beam power P and radius w, my supervisor Dr Rose Ahlefeldt measured the power in the beam as a razor blade incrementally cut off more of the beam. The measured power at a detector is the integral of the intensity profile over the detected area. I fit the power data with an error function (which is the partial integral of a Gaussian), and calculated that the beam before the lens into the cryostat had a radius of 425 ± 4 μm. Assuming the beam was collimated at this point, this would correspond to a waist of 43.7 ± 0.4 μm within the crystal sample after being focused by an $f = 10$ cm lens. Before each oscillator strength pulse sequence, I measured the power in the beam so that I could calculate the field amplitude

and thus the oscillator strengths of the transition.

To extract the Rabi frequency from my echo signal evolution as a function of pulse length, I needed to include the two-pulse echo area model from Equations (3.10) and (3.14) into an equation describing the detected heterodyne signal. The Rigol spectrum analyser detects a signal S that is proportional to the echo amplitude A_e and local oscillator amplitude A_{LO} integrated across the beam. Assuming that the entire beam is coupled into the local oscillator and signal fibres respectively, the detected signal would be given by

$$S \propto \int_0^\infty dr \cdot r A_e A_{LO}. \tag{6.1}$$

I assumed that the echo amplitude A_e was proportional to the echo area model θ_e, and that the local oscillator had the same Gaussian spatial amplitude profile as the signal beam (which is a valid assumption, as both beams were mode matched in the same optical fibres at detection). From these assumptions, I made a model for the spectrum analyser signals given by

$$S = C \int_0^\infty dr \cdot r\theta_e \exp\left(-\frac{r^2}{w(z)^2}\right), \tag{6.2}$$

where C is a scaling constant and θ_e is given by Equation (3.10) or (3.14) for signals from the main or satellite lines respectively, and can be used to extract the Rabi frequency as described in Section 3.4.1. To fit this model to my detected signals, I numerically integrated the model across a wide parameter space based on the parameters of the system (such as the measured coherence times from echo decays, pulse delay times, and absorbance on the main lines) and used an interpolating function over this space to fit to the data.

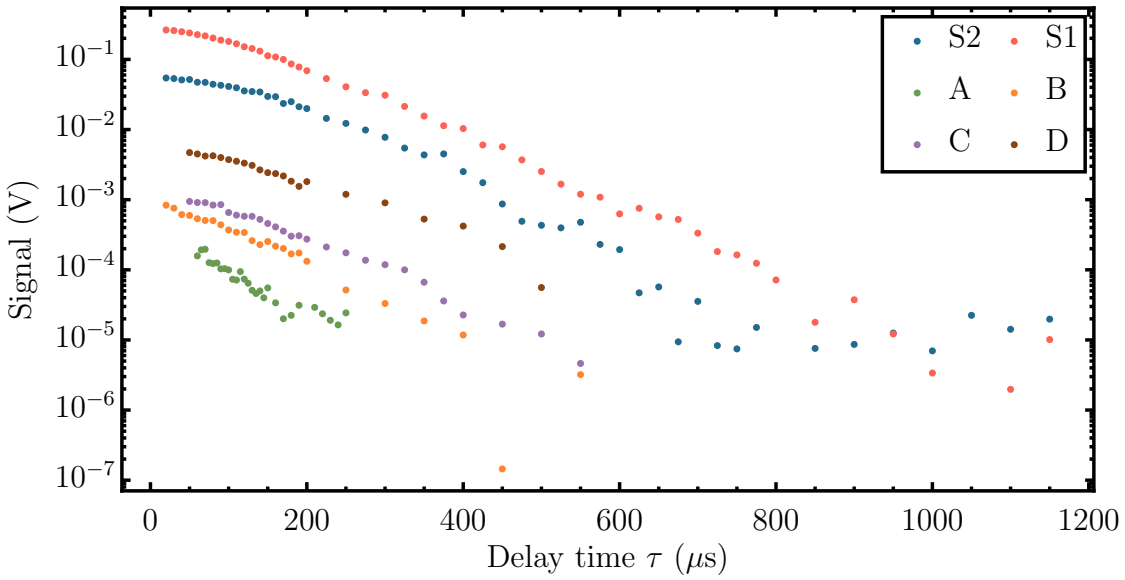

Figure 6.1: Each recorded echo amplitude decay plotted on the same axes to show the sizes of the detected signals for each line.

6.2 Results

6.2.1 Echo decays

Each two-pulse photon echo is shown in Figure 6.1, plotted on the same axes to give an indication of the relative signal strengths for the satellite lines. Interestingly, the echo signals from lines C and D are more intense than line B, despite having smaller peak heights in emission. The potential causes for this is discussed in Section 6.2.2.

From the echo decays in Figure 6.1, the decays on the main lines show a clear non-exponential decay that is indicative of spectral diffusion. For the purposes of calculating oscillator strengths by the technique described in Section 3.4.1 with Equation (3.10), there just needs to be a term that describes the decay of the echo amplitudes. For this purpose, I chose the Mims empirical model [48], which introduces an extra fitting parameter χ, and is given by

$$A(2\tau) \propto \exp\left[-\left(\frac{2\tau}{T_M}\right)^{\chi}\right], \tag{6.3}$$

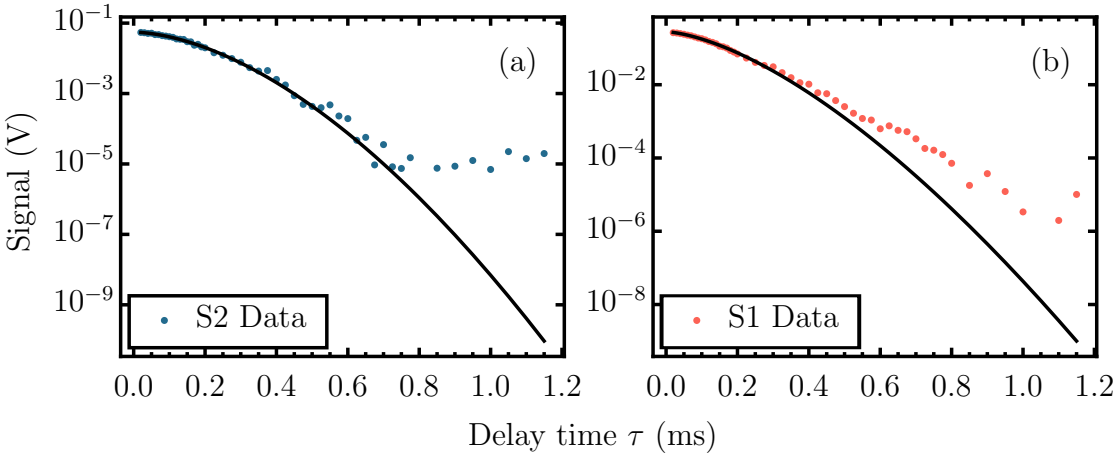

Figure 6.2: The echo amplitude decays on the main lines, fitted with Mims empirical model (black lines) to account for spectral diffusion. The noise floor of the detector of approximate -50 dBm is why the decays suddenly deviate from the fit.

Line	A (V)	T_M (μs)	χ
S1	0.278 ± 0.002	334 ± 3	1.54 ± 0.03
S2	0.0553 ± 0.0005	399 ± 4	1.72 ± 0.04

Table 6.1: The fitting parameters for the echo amplitude decays on the main lines shown in Figure 6.2. A is a proportionality constant.

where χ is an empirical fitting parameter, and T_M is an effective coherence time.

The results of fitting this model to the echo amplitude decays at Site 1 and 2 are shown in Figure 6.2, where the fitting parameters are shown in Table 6.1.

The small uncertainties in the fitting parameters in Table 6.1 show that the data is well fit by this model. These parameters can then be used as constraints for fitting the numerical simulation of the echo amplitude evolution given by Equation (6.2) to calculate the oscillator strengths of the main lines, shown in Section 6.2.2.

While the main lines could not be fit by a straight exponential decay, the echo amplitude decays on the satellite lines are well fit by the expected two-pulse photon echo amplitude of Equation (3.8). Figure 6.3 shows the results of fitting this model to the decays, and Table 6.2 shows the fitting parameters of this process, which gives us a measurement for the coherence time T_2 of the

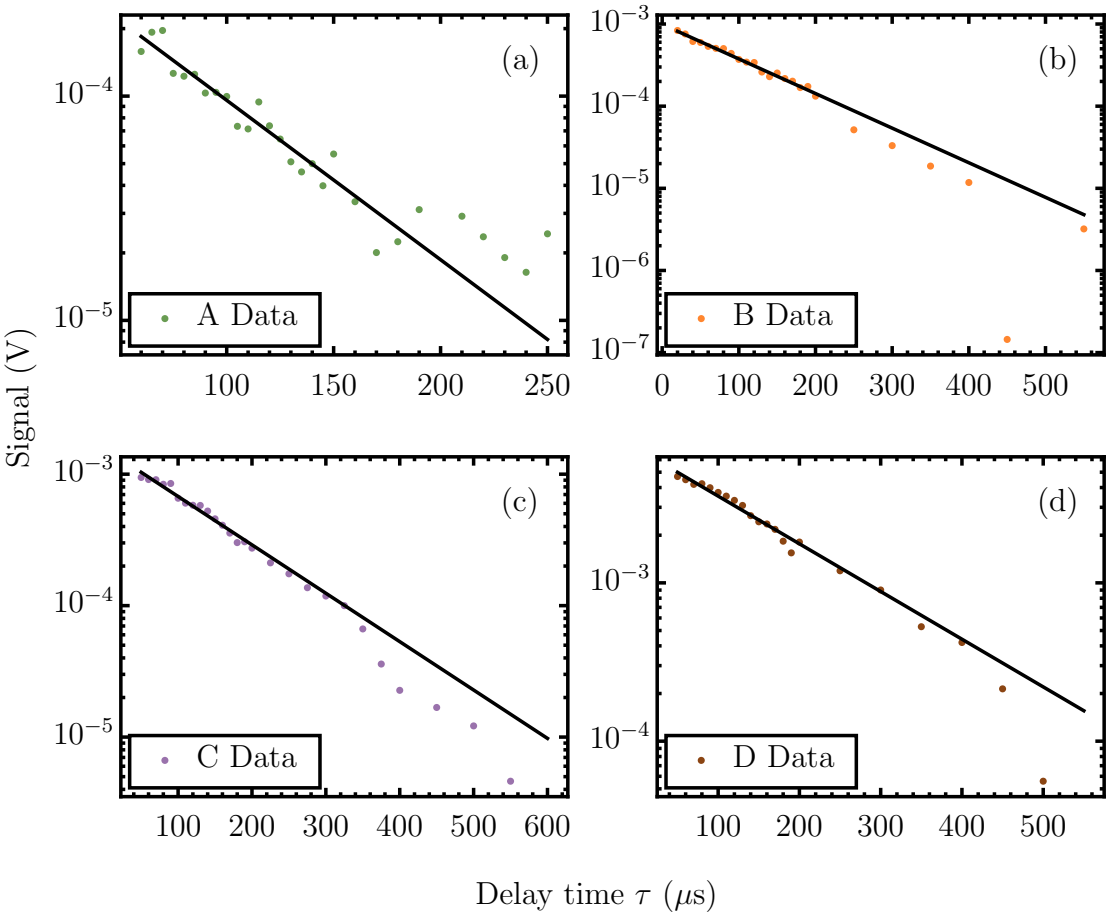

Figure 6.3: The echo amplitude decays on the satellite lines, fitted with a straight exponential decay (black lines) to measure the coherence time T_2.

transition.

While the coherence times T_2 for the satellite lines seem significantly smaller than those of the main lines, this could be a feature of the Mims model fitting. The T_2 values on the satellite lines can be used as constrained parameters for the oscillator strength calculations of the satellite lines.

6.2.2 Oscillator strengths

The results of fitting the numerical interpolation model generated by Equation (6.2) to the main lines is shown in Figure 6.4, where the fitting parameters are shown in Table 6.3.

Line	A (mv)	T_2 (μs)
A	0.49 ± 0.05	122 ± 9
B	0.99 ± 0.02	206 ± 6
C	1.58 ± 0.05	236 ± 9
D	7.07 ± 0.2	299 ± 11

Table 6.2: The fitting parameters for the echo amplitude decays on the satellite lines shown in Figure 6.3. A is a proportionality constant.

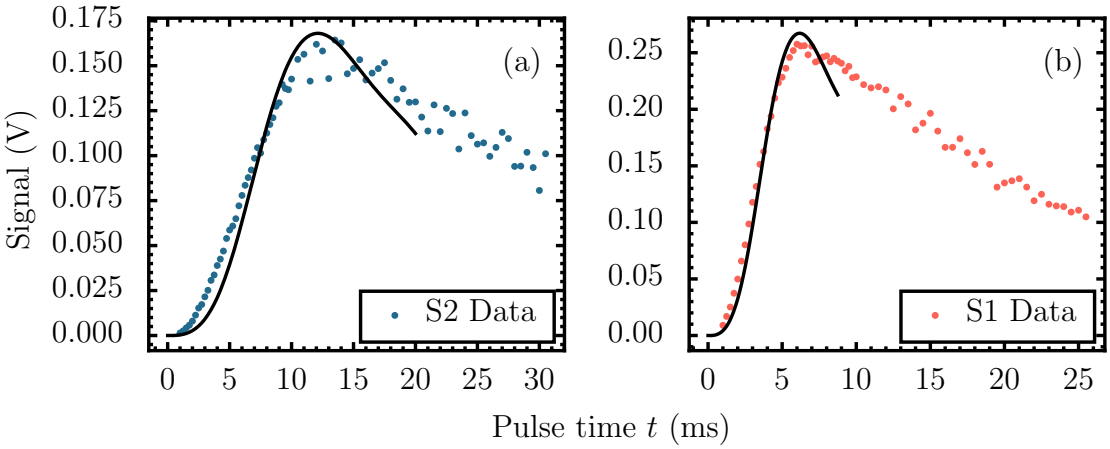

Figure 6.4: The echo area evolution on the main lines, fitted with the numerical model (black lines).

Qualitatively from Figure 6.4, the model does not appear to be a good fit to the data, and this is supported by the large uncertainties for some of the fitting parameters shown in Table 6.3. However, the model does peak at roughly the same location as the data does, which is theoretically when $\Omega t = \pi$, and the uncertainties in the Rabi frequency fitting parameters are small, which suggests that the Rabi frequency fitting parameters should be suitable for calculating oscillator strengths of the transitions for comparison with the oscillator strengths of the satellite lines.

Similarly, the results of fitting the numerical interpolation model generated by Equation (6.2) to the satellite lines is shown in Figure 6.5, where the fitting parameters are shown in Table 6.4.

Line	A (V)	Ω (kHz)	αz	T_M (μs)	χ
S1	4 ± 100	720 ± 40	0.4 ± 0.8	336 ± 0.7	2 ± 100
S2	2 ± 40	370 ± 20	0.4 ± 0.7	402 ± 0.4	2 ± 90

Table 6.3: The fitting parameters for the echo area evolution on the main lines shown in Figure 6.4.

Line	A (mV)	Ω (kHz)	T_2 (μs)
A	2.09 ± 0.06	474 ± 13	$123 \pm 9 \times 10^{-9}$
B	5.42 ± 0.2	494 ± 13	$206 \pm 8 \times 10^{-9}$
C	6.69 ± 0.2	687 ± 11	$236 \pm 9 \times 10^{-9}$
D	28.9 ± 1	702 ± 15	$288 \pm 8 \times 10^{-8}$

Table 6.4: The fitting parameters for the echo area evolution on the satellite lines shown in Figure 6.5.

Qualitatively from Figure 6.5, the model seems like a much better fit for the satellite lines than the main line. In addition, the fitting parameters in Table 6.4 have much more reasonable uncertainties than in Table 6.3, apart from in the T_2 column. As such, the Rabi frequencies can be used to calculate the oscillator strength of the transitions.

By using the measured power in the beam for each oscillator strength data set, and the calculated beam waist within the crystal from the beam profiling, the Rabi frequencies and electric field (which is the square root of the Gaussian beam intensity profile) can be substituted into Equation (3.5) and subsequently (3.9) to calculate the oscillator strength of each of the transitions. These calculated oscillator strengths are shown in Table 6.5 and plotted in Figure 6.6.

From Figure 6.6, there appears to be two clusters of oscillator strength values, where lines A and B have similar oscillator strengths to S2, and lines C and D have similar oscillator strengths to S1. This suggests that the oscillator strength of a transition could be used to associate satellite lines to pair sites.

As I briefly mentioned in Section 6.2.1, the echo decay signals from lines C and

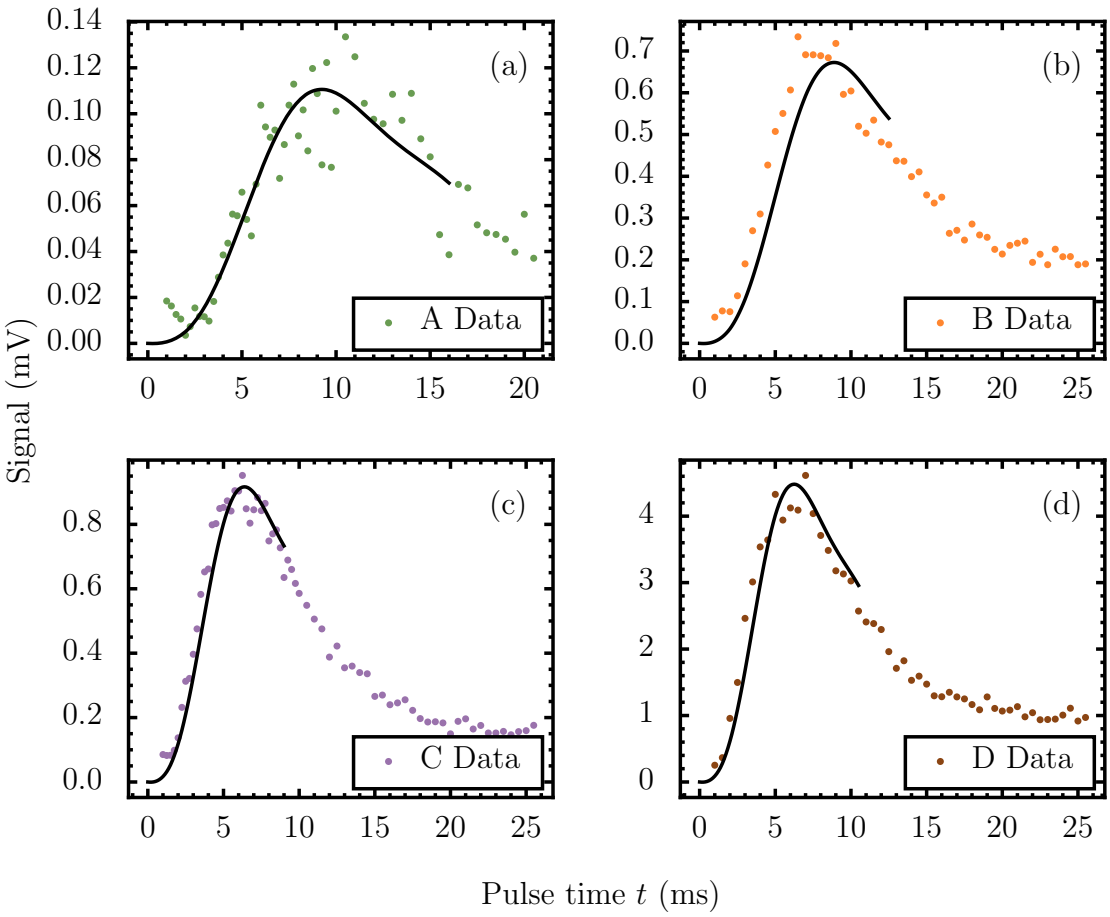

Figure 6.5: The echo area evolution on the satellite lines, fitted with the numerical model (black lines).

D were stronger than those from B, despite being significantly smaller peaks in emission. The stronger echo signals can be explained by C and D being stronger oscillators. However, this is particularly interesting for line C, as it is overlapped with line B (Figure 5.2). This has two potential explanations.

The simplest explanation of the different oscillator strengths for line B and C is that B is associated with S2, C is associated with S1, and they happen to overlap in frequency. An alternative option could be that B is an S1 coupled pair with a suppressed oscillator strength due to degenerative pair coupling. What this means is that the coupled interaction is stronger than the inhomogeneous broadening of the satellite lines, which could be used for high fidelity quantum gates.

Line	Oscillator strength
S1	3.4×10^{-6}
S2	0.92×10^{-6}
A	1.4×10^{-6}
B	1.5×10^{-6}
C	2.9×10^{-6}
D	3.0×10^{-6}

Table 6.5: The calculated oscillator strength of the transition in each line.

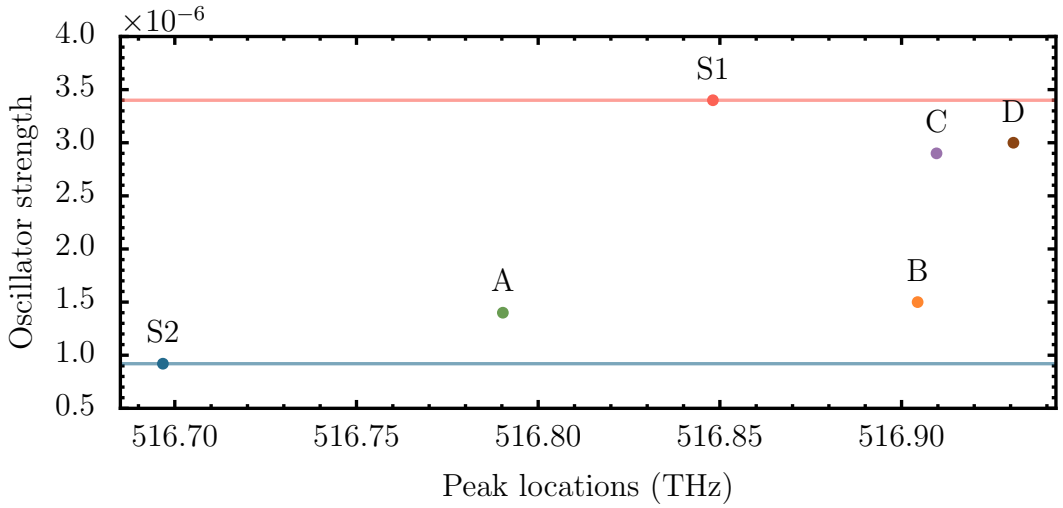

Figure 6.6: The calculated oscillator strengths of the main (S1, S2) and satellite (A-D) lines in Eu^{3+}:Y_2SiO_5.

In summary, I recorded two pulse photon echo measurements on the main and satellite lines of Eu^{3+}:Y_2SiO_5. I measured the coherence times T_2 of the satellite lines A-D, which are presented in Table 6.2, and has not been done before. I also recorded the oscillator strengths of the satellite lines and main lines, and determined that this could be one method of allocating satellite lines to pair sites.

Chapter 7

Conclusion

In this thesis, I studied the spectral and coherent properties of satellite lines in 0.1% Eu^{3+}:Y_2SiO_5 crystals. The aim of the project was to conduct basic spectroscopy measurements on the satellite lines to evaluate their potential for two-qubit gates, and to associate satellite lines to pair sites.

In this project, I recorded wide, high resolution, polarisation dependent excitation spectra of the $^7F_0 \rightarrow {}^5D_0$ transition of Eu^{3+} to determine if this method could be used to associate satellite lines to pair sites. I concluded that this method could not be used to associate satellite lines to pair sites. Additionally, I investigated whether the peak heights of satellite lines were present in the expected ratios given by the symmetries of the sites. I concluded that they were not which, in conjunction with the polarisation measurements, indicates the pair sites are strongly perturbed compared to isolated ions in Eu^{3+}:Y_2SiO_5. Through this investigation, I mapped the precise locations of satellite lines in the spectrum of Eu^{3+}:Y_2SiO_5, which has not been done before.

I measured the optical coherence times of four satellite lines in Eu^{3+}:Y_2SiO_5. The coherence times were 122 ± 9 μs, 206 ± 6 μs, 236 ± 9 μs and 299 ± 11 μs. The presence of instantaneous spectral diffusion in the coherence measurements on the main lines meant that it was not possible to make a direct comparison between these values and those on the satellite lines.

I measured the oscillator strengths of the main lines and the four satellite lines mentioned above. Each satellite line had an oscillator strength close to that

of one of the main lines. From this, it is possible that oscillator strengths could be used to associate satellite lines to pair sites.

In this project, I also stabilised the new Toptica TA-SHG pro laser purchased by the rare earth ion group at ANU for quantum gate operations. The laser is now stable enough to begin investigating two-qubit gate operations in this system.

While I was able to measure the coherence times of satellite lines in this project, I was not able to do it with a stabilised laser, as incorporating an electro-optic modulator into the setup for frequency control of the stabilised laser made it difficult to detect signals from the weak satellite lines. The next steps for this project are incorporating an electro-optic modulator back into the setup, as this will be necessary for any demonstration of a two-qubit gate in this system.

In the excitation spectrum of Eu^{3+}:Y_2SiO_5, there were multiple instances of two satellite lines just resolved from each other over their inhomogeneous broadening. Two of the satellite lines where the oscillator strengths were measured were in this configuration, where one had approximately double the oscillator strength of the other. Interestingly, the line with the greater oscillator strength had the weakest emission. A possible explanation is that the two satellite lines are caused by identical sites, where a resonant interaction results in delocalised states that are resolved beyond the inhomogeneous broadening. To determine if they are caused by this, a Raman heterodyne spectrum of the two lines could reveal if the hyperfine structure is very different compared to other satellite lines. Additionally, a large magnetic field could be applied to the sample to induce Zeeman splitting, revealing if the sites were or weren't degenerate.

Bibliography

[1]M. A. Nielsen and I. L. Chuang, *Quantum Computation and Quantum Information: 10th Anniversary Edition* (Cambridge University Press, 2010).

[2]D. Deutsch, "Quantum theory, the Church-Turing principle and the universal quantum computer", Proceedings of the Royal Society of London. A. Mathematical and Physical Sciences **400**, 97–117 (1985).

[3]P. W. Shor, "Polynomial-time algorithms for prime factorization and discrete logarithms on a quantum computer", SIAM review **41**, 303–332 (1999).

[4]R. P. Feynman, "Simulating physics with computers", International Journal of Theoretical Physics **21**, 467–488 (1982).

[5]P.-H. Wang, J.-H. Chen, Y.-Y. Yang, C. Lee, and Y. J. Tseng, "Recent Advances in Quantum Computing for Drug Discovery and Development", IEEE Nanotechnology Magazine **17**, 26–30 (2023).

[6]C. H. V. Cooper, "Exploring Potential Applications of Quantum Computing in Transportation Modelling", IEEE Transactions on Intelligent Transportation Systems **23**, 14712–14720 (2022).

[7]M. Zhong, M. P. Hedges, R. L. Ahlefeldt, J. G. Bartholomew, S. E. Beavan, S. M. Wittig, J. J. Longdell, and M. J. Sellars, "Optically addressable nuclear spins in a solid with a six-hour coherence time", Nature **517**, 177–180 (2015).

[8]M. Rančić, M. P. Hedges, R. L. Ahlefeldt, and M. J. Sellars, "Coherence time of over a second in a telecom-compatible quantum memory storage material", Nature Physics **14**, 50–54 (2018).

[9]N. Ohlsson, R. Krishna Mohan, and S. Kröll, "Quantum computer hardware based on rare-earth-ion-doped inorganic crystals", Optics Communications **201**, 71–77 (2002).

[10]K. Ichimura, "A simple frequency-domain quantum computer with ions in a crystal coupled to a cavity mode", Optics Communications **196**, 119–125 (2001).

[11]R. L. Ahlefeldt, "Evaluation of a stoichiometric rare earth crystal for quantum computing", PhD thesis (Laser Physics Centre, Research School of Physics and Engineering, The Australian National University, 2013).

[12]M. Pearce, "Quantum gate optimisation in stoichiometric rare-earth ensembles", MA thesis (Department of Quantum Science and Technology, Research School of Physics, The Australian National University, 2022).

[13]D. P. DiVincenzo, "The Physical Implementation of Quantum Computation", Fortschritte der Physik **48**, 771–783 (2000).

[14]R. L. Ahlefeldt, M. J. Pearce, M. R. Hush, and M. J. Sellars, "Quantum processing with ensembles of rare-earth ions in a stoichiometric crystal", Phys. Rev. A **101**, 012309 (2020).

[15]M. J. Sellars, E. Fraval, and J. J. Longdell, "Investigation of static electric dipole-dipole coupling induced optical inhomogeneous broadening in Eu^{3+}:Y_2SiO_5", Journal of Luminescence **107**, 150–154 (2004).

[16]M. Yamaguchi, K. Koyama, T. Suemoto, and M. Mitsunaga, "Mapping of site distribution in Eu^{3+}:$YAlO_3$ on RF-optical frequency axes by using double-resonance spectroscopy", Journal of Luminescence **76-77**, Proceedings of the Eleventh International Conference on Dynamical Processes in Excited States of Solids, 681–684 (1998).

[17]J. J. Longdell, M. J. Sellars, and N. B. Manson, "Demonstration of Conditional Quantum Phase Shift Between Ions in a Solid", Phys. Rev. Lett. **93**, 130503 (2004).

[18]J. H. Wesenberg, K. Mølmer, L. Rippe, and S. Kröll, "Scalable designs for quantum computing with rare-earth-ion-doped crystals", Phys. Rev. A **75**, 012304 (2007).

[19]A. Kinos, L. Rippe, S. Kröll, and A. Walther, "Designing gate operations for single-ion quantum computing in rare-earth-ion-doped crystals", Phys. Rev. A **104**, 052624 (2021).

[20]R. L. Ahlefeldt, D. L. McAuslan, J. J. Longdell, N. B. Manson, and M. J. Sellars, "Precision Measurement of Electronic Ion-Ion Interactions between Neighboring Eu^{3+} Optical Centers", Phys. Rev. Lett. **111**, 240501 (2013).

[21]R. D. Shannon and C. T. Prewitt, "Effective ionic radii in oxides and fluorides", Acta Crystallographica Section B **25**, 925–946 (1969).

[22]G. Liu, "Electronic Energy Level Structure", in (Jan. 2006), pp. 1–94.

[23]Y. C. Sun, "Rare Earth Materiais in Optical Storage and Data Processing Applications", in *Spectroscopic Properties of Rare Earths in Optical Materials*, edited by R. Hull, J. Parisi, R. M. Osgood, H. Warlimont, G. Liu, and B. Jacquier (Springer Berlin Heidelberg, Berlin, Heidelberg, 2005), pp. 379–429.

[24]M. Zhong, "Development of Persistent Quantum Memories", PhD thesis (Laser Physics Centre, Research School of Physics and Engineering, The Australian National University, 2017).

[25]B. R. Judd, "Optical Absorption Intensities of Rare-Earth Ions", Phys. Rev. **127**, 750–761 (1962).

[26]G. S. Ofelt, "Intensities of Crystal Spectra of Rare-Earth Ions", The Journal of Chemical Physics **37**, _eprint: https://pubs.aip.org/aip/jcp/article-pdf/37/3/511/10988010/511_1_online.pdf, 511–520 (2004).

[27]R. Macfarlane and R. Shelby, "CHAPTER 3 - Coherent Transient and Hole-burning Spectroscopy of Rare Earth Ions in Solids", in *Spectroscopy of Solids Containing Rare Earth Ions*, Vol. 21, edited by A. Kaplyanskii and R. Macfarlane, Modern Problems in Condensed Matter Sciences (Elsevier, 1987), pp. 51–184.

[28]F. Könz, Y. Sun, C. W. Thiel, R. L. Cone, R. W. Equall, R. L. Hutcheson, and R. M. Macfarlane, "Temperature and concentration dependence of optical dephasing, spectral-hole lifetime, and anisotropic absorption in Eu^{3+}: Y_2SiO_5", Phys. Rev. B **68**, 085109 (2003).

[29]R. Yano, M. Mitsunaga, and N. Uesugi, "Ultralong optical dephasing time in Eu3+:Y2SiO5", Opt. Lett. **16**, 1884–1886 (1991).

[30]R. Yano, M. Mitsunaga, and N. Uesugi, "Nonlinear laser spectroscopy of Eu3+:Y2SiO5 and its application to time-domain optical memory", J. Opt. Soc. Am. B **9**, 992–997 (1992).

[31]R. S. Meltzer, "Line Broadening Mechanisms and Their Measurement", in *Spectroscopic Properties of Rare Earths in Optical Materials*, edited by R. Hull, J. Parisi, R. M. Osgood, H. Warlimont, G. Liu, and B. Jacquier (Springer Berlin Heidelberg, Berlin, Heidelberg, 2005), pp. 191–265.

[32]R. Jaaniso, H. Hagemann, and H. Bill, "Inhomogeneous broadening of optical spectra in mixed crystals: Basic model and its application to Sm^{2+} in $SrFCl_xBr_{1-x}$", The Journal of Chemical Physics **101**, 10323–10337 (1994).

[33]M. Pelletier and C. Pelletier, "RAMAN SPECTROSCOPY — Instrumentation", in *Encyclopedia of Analytical Science (Second Edition)*, edited by P. Worsfold, A. Townshend, and C. Poole, Second Edition (Elsevier, Oxford, 2005), pp. 94–104.

[34]C. Burgess, "OPTICAL SPECTROSCOPY — Detection Devices", in *Encyclopedia of Analytical Science (Second Edition)*, edited by P. Worsfold, A. Townshend, and C. Poole, Second Edition (Elsevier, Oxford, 2005), pp. 438–443.

[35]R. L. Shoemaker, "Coherent Transient Effects in Optical Spectroscopy", Annual Review of Physical Chemistry **30**, 239–270 (1979).

[36]M. J. Sellars, "Ultra-High Resolution Laser Spectroscopy of Rare Earth Doped Solids", PhD thesis (Research School of Physics, The Australian National University, 1995).

[37]A. Kälin, R. Kesselring, C. Hongru, and F. Kneubühl, "Optical free induction decay (OFID) 10 μm CO_2 laser systems", Infrared Physics **33**, 73–112 (1992).

[38]R. G. Brewer and R. L. Shoemaker, "Optical Free Induction Decay", Phys. Rev. A **6**, 2001–2007 (1972).

[39]T. Muramoto, S. Nakanishi, and T. Hashi, "Coherent transients observed by Stark switching in ruby having narrow optical hole burning", Optics Communications **24**, 316–320 (1978).

[40]G. J. Pryde, "Ultrahigh resolution spectroscopic studies of optical dephasing in solids", PhD thesis (Research School of Physics, The Australian National University, 1999).

[41]R. Urmancheev, K. Gerasimov, M. Minnegaliev, T. Chanelière, A. Louchet-Chauvet, and S. Moiseev, "Two-pulse photon echo area theorem in an optically dense medium", Opt. Express **27**, 28983–28997 (2019).

[42]S. L. McCall and E. L. Hahn, "Self-Induced Transparency", Phys. Rev. **183**, 457–485 (1969).

[43]R. Paschotta, *Gaussian Beams*, Sept. 2023.

[44]*Gaussian Beam Propagation*, Sept. 2023.

[45]H. R. Carleton and W. T. Maloney, "A Balanced Optical Heterodyne Detector", Appl. Opt. **7**, 1241–1243 (1968).

[46]R. Stierlin, R. Bättig, P. .-. Henchoz, and H. P. Weber, "Excess-noise suppression in a fibre-optic balanced heterodyne detection system", Optical and Quantum Electronics **18**, 445–454 (1986).

[47]R. W. P. Drever, J. L. Hall, F. V. Kowalski, J. Hough, G. M. Ford, A. J. Munley, and H. Ward, "Laser phase and frequency stabilization using an optical resonator", Applied Physics B **31**, 97–105 (1983).

[48]W. B. Mims, "Phase Memory in Electron Spin Echoes, Lattice Relaxation Effects in $CaWO_4$: Er, Ce, Mn", Phys. Rev. **168**, 370–389 (1968).